4. Electron Transfer and Solvation at Ice – Metal Interfaces

In this chapter, results on the electron transfer and solvation dynamics at the $D_2O/Cu(111)$ and $D_2O/Ru(001)$ interfaces are presented. It will be shown that both, the substrate and the structure of the ice layer, have considerable impact on the interfacial electron dynamics. For example, the transition from the metastable amorphous structure of the ice layer to the crystalline phase is governed by a drastic change of the timescales on which solvation and transfer occur. The first section deals with the ultrafast dynamics at amorphous ice-metal interfaces and the influence of the substrate and of the ice morphology on the electron transfer and solvation dynamics is discussed. The strong coupling of the solvated electrons to the metal states leads here to charge transfer times on femtosecond timescales, so that the excited electrons decay back to the substrate before they equilibrate with their surrounding. In the case of crystalline ice (section 4.2) electrons are trapped for minutes in the adlayer at a nanometer distance from the metal substrate. This "freezing" of the initially hot electrons is enabled by a significantly stronger screening of the excess charge from the metal surface: The electronic wave function is only weakly coupled to the substrate states.

4.1 Ultrafast Electron Dynamics at Amorphous Ice-Metal Interfaces

As discussed in chapter 2, the interfacial solvated electron is a model system for charge transfer processes at interfaces due to its transient degree of confinement: The coupling strength of the solvated electron to substrate states changes with ongoing solvation so that deeper insight into the underlying fundamental processes may be gained by a systematic investigation of the transfer dynamics at different stages of solvation. The first paragraph discusses in how far the electron coupling is influenced by the substrate. Then, in paragraph 4.1.2, the impact of the ice morphology is investigated. To achieve a complete picture of the transfer and solvation dynamics, paragraph 4.1.3 addresses the question of whether the electrons solvate at the ice-vacuum interface or in the bulk of the adsorbed water. Finally, the findings will be discussed on the basis of the charge transfer theories introduced in chapter 2.

4.1.1 Cross-Over between Substrate- and Barrier-Determined ET

The fundamental steps of electron transfer and solvation dynamics at the amorphous $D_2O/Cu(111)$ were introduced in paragraph 2.3.1. Two spectral features were observed for this interface, a broad, short-lived continuum, which was attributed to the ice conduction band (e_{CB}) and a sharp peak, e_S, shifting down to lower energies with increasing time delay, which was assigned to solvated electrons in the ice adlayer. Selected, time-dependent spectra are plotted in the inset of Fig. 4.01 as a function of intermediate state energy (top axis) and time delay (right axis). It was concluded that charge injection occurs via the delocalized conduction band of the ice layer and that the subsequent stabilization of the excess electron is reflected by the peak shift of the e_S maximum. The electron population in the ice layer decreases with increasing time delay as the solvated electrons decay back to the metal substrate.
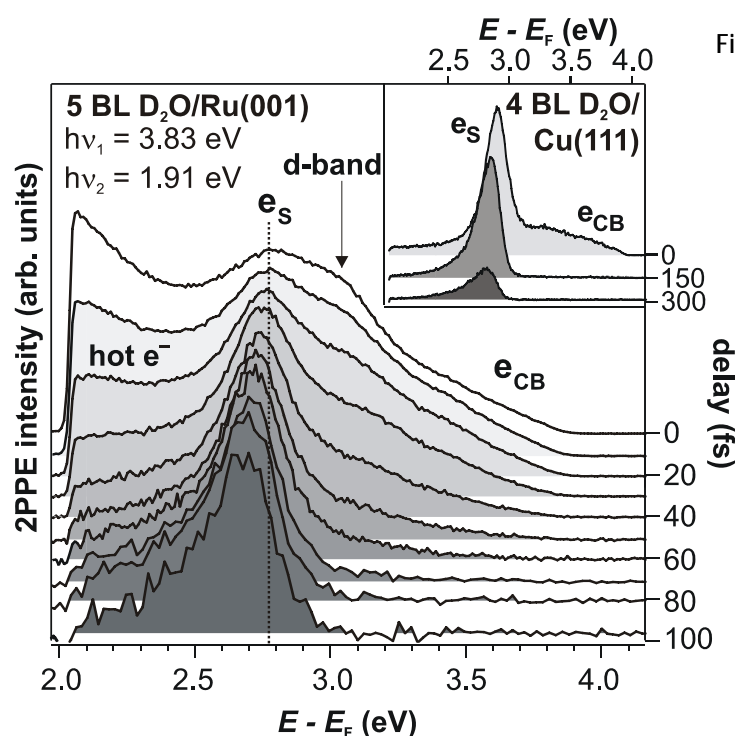

Fig. 4.01: *Time-Resolved 2PPE Spectra of Amorphous D_2O on Metal Surfaces.* Inset: 2PPE spectra of 4 BL $D_2O/Cu(111)$ at three different time delays. The short-lived continuum e_{CB} results from delocalized conduction band electrons. The solvated electron peak e_S exhibits a finite lifetime and shifts to lower energies with increasing time delay. Main panel: In addition to the strong background signal of hot electrons and d-bands, the spectra show qualitatively the same electron dynamics: A broad, short-lived continuum (e_{CB}) and a peak shifting to lower energies with increasing time delay (e_S). The maximum of e_S was normalized in all spectra to make recognition of the peak shift easier (data adopted from [Gah04] and [Stä04]).

Fig. 4.01 depicts time-resolved 2PPE spectra of a 5 BL thick film of amorphous D_2O on the Ru(001) surface.[63] Although the spectra appear to be different compared with the $D_2O/Cu(111)$ data (inset), they show qualitatively the same interfacial electron dynamics as in the case of ice on Cu(111). Differences in the spectra result from the considerably higher DOS of the Ru(001) substrate (cf. Fig. 2.21): The spectra exhibit notable contributions from the metal template. The high signal at the secondary edge ($E - E_F > 2$ eV) results from hot electrons close to the Fermi Level of Ru(001), and the shoulder at ~ 3 eV is due to the

---

[63] As the electron dynamics do not change as a function of layer thickness for $D_2O/Cu(111)$ above 3 BL [Gah03] it is possible to compare the data of the inset with the main panel.

unoccupied d-bands of the substrate. Both features have already been discussed on the basis of Fig. 3.14. As these signals result from an excitation by visible light and probed by UV photons,[64] their dynamics (to negative delays, not shown) do not superpose with the solvated electron dynamics. Besides these background signals the qualitative electron dynamics are similar to the $D_2O/Cu(111)$ case: A broad, short-lived continuum is observed, which is attributed to the ice conduction band, and a peak with a finite lifetime that shifts down to lower energies with increasing time delay, which is originating from solvated electrons.

To quantify the differences between the $D_2O/Cu(111)$ and the $D_2O/Ru(001)$ system it is appropriate to compare the energy shifts of the peak maximum of e_S for both substrates, depicted in Fig. 4.02.[65] At $t = 0$ fs the peak for $D_2O/Ru(001)$ (green circles) lies 100 meV lower in energy (at 2.8 eV) than for Cu(111). This difference is due to the different work functions of the two systems: 3.9 eV for $D_2O/Cu(111)$ and 3.8 eV for $D_2O/Ru(001)$. Hence, the binding energy of e_S with respect to the respective vacuum level is similar for both templates right after photoinjection. It is apparent from Fig. 4.02 that e_S shifts with a considerably higher rate for Ru(001) than for the $D_2O/Cu(111)$ system (orange diamonds). Linear fits to the data (dashed lines) give energy shifts of $\Sigma_S^{Cu} = -0.27$ eV/ps and $\Sigma_S^{Ru} = -0.83$ eV/ps, respectively. The energetic shift of the maximum of the solvated electron distribution is hence significantly influenced by the substrate used. However, the origin of this difference (e.g. substrate's electronic band structure, mobility of the molecules) is not obvious. As the peak shift occurs simultaneously with the population decay of the solvated electrons back to the metal substrate (cf. 2.3.1), interpretation of Fig. 4.02 has to incorporate the population dynamics. As mentioned
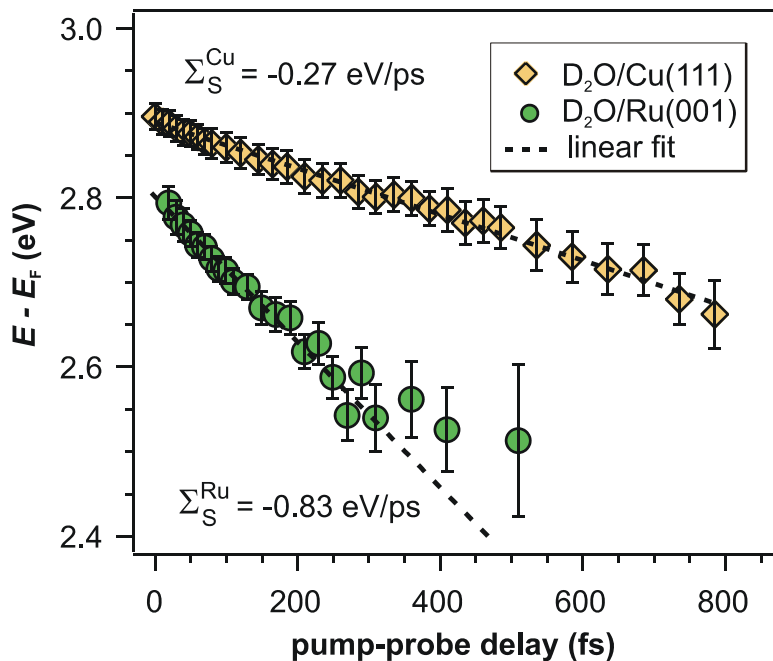

Fig. 4.02: *Energetic Shift of e_S for $D_2O/Cu(111)$ and Ru(001).* According to the linear fits (dashed lines) the peak maximum shifts in the case of the ice-Ru system (green circles) three times faster than for $D_2O/Cu(111)$ (orange diamonds).

---

[64]Their intermediate state energy is by $\Delta h\nu = 1.92$ eV lower than depicted by the bottom axis.

above, the transfer probability varies with increasing energetic stabilization of the excess electrons, because the reorientation of the water molecules leads to an increased screening of the solvated electrons from the metal substrate. Hence, the evaluation of the e_S population decay to *both* employed substrates is required before conclusions may be drawn from the different peak shifts observed in Fig. 4.02.

The transients of the solvated electron population for D_2O on Cu(111) and on Ru(001) result from the integration of the 2PPE intensity in the energy interval of the electron solvation dynamics, i.e. 2.4 – 2.8 eV and 2.4 – 2.9 eV for Ru(001) and Cu(111), respectively. The resulting normalized cross correlation traces of pump and probe pulse are presented in Fig. 4.03. At early times (t < 300 fs) the population decay of the solvated electrons clearly differs for Cu(111) (orange diamonds) and Ru(001) (green circles). The single-exponential fits[66] (dotted curves) give initial decay times of $\tau_1^{Cu} = 140(5)$ fs and $\tau_1^{Ru} = 34(5)$ fs, i.e. the solvated electrons decay at early delays four times faster to the Ru(001) substrate than to the Cu(111) crystal. The fits reproduce the experimental data up to 150 and 350 fs for Ru and Cu, respectively. At later delays a significant slowing down of the population decay leads to deviations from the exponential behavior.
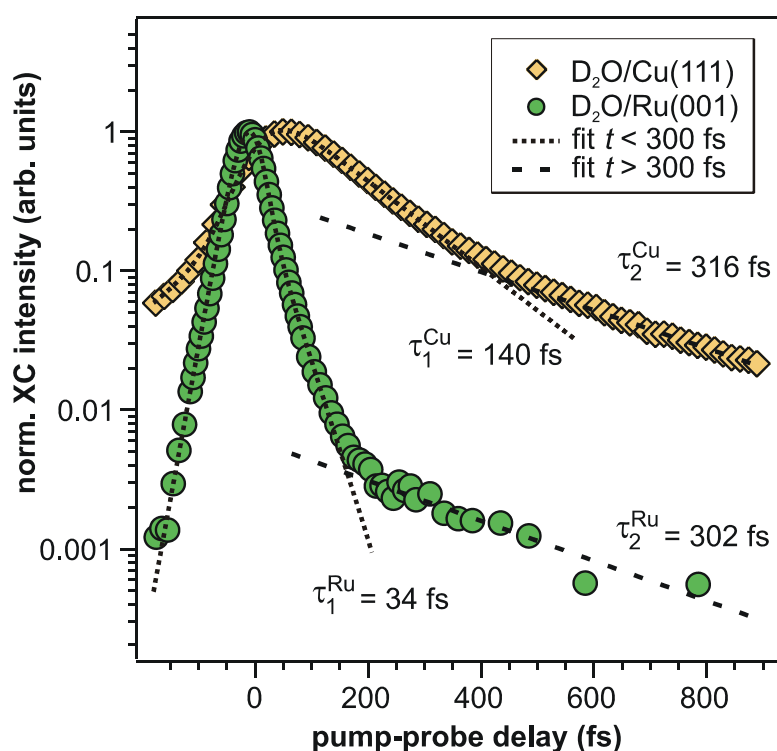

Fig. 4.03: *Population Decay of e_S for D_2O/Cu(111) and Ru(001).* At early delays (t < 300 fs) the electron back transfer times differ significantly for the two substrates. At large delays the transfer dynamics slow down and the gradient of the transients becomes similar. Dashed and dotted curves are single-exponential decays fitted to the data.

[65] Due to the strong, time-dependent background, the peak maxima were manually determined from the 2PPE dataset shown in Fig. 4.01.
[66] As discussed in 3.4.2, the exponential is convolved with the respective laser pulse envelope. The contribution of hot electrons is taken into account by another exponential decay towards negative delays.

In addition to the slowing down of the population decay, which occurs for both substrates, the respective transfer times become comparable for delay times larger than 300 fs (Fig. 4.03). To quantify the decay times additional exponential fits are required. To ensure comparability of the data, the energetic shift of the e_S maximum has to be taken into account. It is suitable to compare the transfer times of electrons that gained the same amount of binding energy since their injection via the ice conduction band. Hence, the time window of $280 - 480$ fs for $D_2O/Ru(001)$ corresponds to $600 - 800$ fs for the ice-Cu system, as the peak maximum shifted in both cases by 0.25(5) eV. The resulting fits give identical transfer times of $\tau_2^{Cu} = 316(20)$ fs and $\tau_2^{Ru} = 302(20)$ fs within the experimental resolution.

It is already obvious from this – rather coarse – data analysis that the population dynamics of the solvated electrons at ice-metal interfaces have to be separated into two regimes: The early time delays, where the decay constants τ_1 of the two substrates differ significantly and the later time delays, where the decay constants τ_2 are identical for Cu(111) and Ru(001). The back transfer appears to be dominated by the substrate's properties in the former case, while – in the latter case – the electron decay seems to become independent of the underlying metal surface.

Early Time Delays ($t < 300$ fs): The solvated electron distribution decays four times faster to the Ru(001) substrate than to the copper crystal. At the same time, the peak maximum shifts to lower energies considerably faster for the $D_2O/Ru(001)$ system. Apparently the choice of substrate has significant influence on the electron dynamics at early time delays. A faster population decay could be explained by: (i) Screening, i.e. solvation of the excess electrons is weaker for $D_2O/Ru(001)$ and hence the coupling and decay to this substrate is enhanced. (ii) The faster decay is due to differences of the substrates surface electronic band structures. As the faster population dynamics are accompagnied by the accelerated peak shift for $D_2O/Ru(001)$, a weaker screening (slower reaction of the molecules, scenario(i)) is improbable. Additionally, the slowing down of the population decay occurs for the Ru(001) substrate already after 150 fs; for Cu(111) it starts at 350 fs (cf. Fig. 4.03). This means that the substrate influence is suppressed for the Ru(001) substrate *earlier* than for Cu(111). Hence, a faster decay for $D_2O/Ru(001)$ cannot be due to a *slower* reaction of the water molecules in this system. Accordingly, the electron transfer dynamics depend at these early times on the surface electronic band structures and densities of states. Thus, this regime of back transfer will be termed *substrate-dominated*, in accordance with section 2.1.1. This nomenclature is justified when comparing the DOS and surface electronic band structures of the two substrates given in Fig. 2.21. The density of states is comparable for Cu and Ru at the energies of the solvated electrons, but differs significantly for energies < 2 eV due to the unoccupied d-bands of ruthenium. The larger phase space for *inelastic* scattering events could be responsible for the faster decay of the $D_2O/Ru(001)$ system. On the other hand, the projected surface electronic band structures also offer an explanation for the fast back transfer: The orientational sp-band gaps of the two substrates differ. While the gap extends from below the Fermi Level up to E_{vac} for Cu(111), the bottom of the gap lies more than 1 eV above E_F for Ru(001). This difference results in a much narrower band gap of Ru(001) in k-space at the energy of the solvated

electrons (cf. Fig. 2.21). As the solvated electrons are localized parallel to the metal surface, they exhibit a corresponding, finite bandwidth in k-space. [Bov03] Thus, as discussed in 2.1.1 and in agreement with present understanding [Bor01], the *elastic* transfer of this localized electron depends on the width Δk_{gap} of the substrate band gap in momentum space. In the case of a solvated electron in an ice layer on Cu(111), the required momentum change for elastic back transfer is larger than for the Ru(001) surface, as transitions into the gap are forbidden. It can be concluded that both, elastic and inelastic electron transfer, may contribute to the faster initial decay for $D_2O/Ru(001)$. The magnitude of the respective contribution certainly depends on the details of the electronic structures and coupling matrix elements.

Later Time Delays ($t > 300$ fs): This regime of electron transfer is characterized by similar transfer times τ_2 for both substrates, which are, additionally, larger than the initial transfer times τ_1. As mentioned in 2.3.1, it could be shown that electron solvation is governed by an increasing wave function constriction, i.e. a barrier formation at the interface due to the enhanced screening of the surrounding molecules. This barrier exhibits a transient height and width that determines the transfer rate at the respective time delay. As soon as the barrier is high and wide enough, the charge transfer probability to the metal will be determined by the tunneling probability through the barrier: At this point, the wave function overlap with the metal states is so significantly reduced that tunneling becomes the rate-limiting step. As back relaxation for $D_2O/Cu(111)$ and Ru(001) slows down significantly and the differences due to substrate variation vanish, the charge transfer regime for $t > 300$ fs is termed *barrier-determined*.

Fig. 4.04 summarizes the above discussion. The observed transfer dynamics for the $D_2O/Cu(111)$ and the $D_2O/Ru(001)$ system can be separated into two regimes. At early delays the solvated electron still exhibits a considerable wave function overlap with metal states so that the transfer time is dominated by the substrates electronic properties (Fig. 4.04a). With ongoing solvation the potential barrier increases and leads to a subsequent reduction of the charge transfer probability. The tunneling through this barrier becomes the rate-limiting step and the electron transfer time is independent of the underlying substrate (Fig. 4.04b)

Fig. 4.04: *Substrate-Dominated and Barrier-Determined Electron Transfer.* a) The wave function overlap of the solvated electron with metal states leads to a strong influence of the substrate's surface electronic band structure on the transfer rate. b) A potential barrier screens the electronic wave function from the metal. Thus, the tunneling probability determines the transfer time.
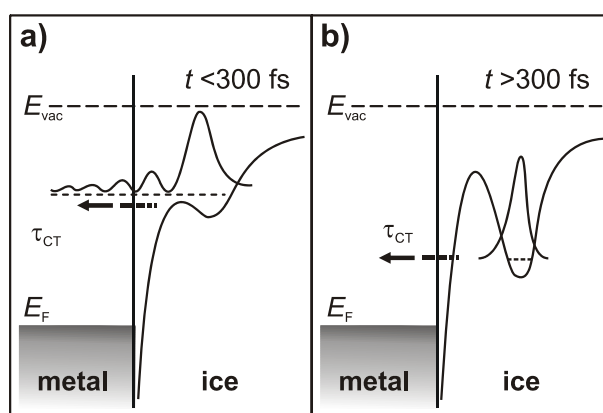
It is important to keep in mind that electron back transfer and energetic stabilization occur simultaneously. Ultimately, it is the solvation that leads to the increase of transfer time and, vice versa, the increased lifetime enables the progression of solvation. In other words, electron back transfer *competes* with solvation: While the former leads to a subsequent population decrease, the latter results in longer-living electrons. It is therefore appropriate to consider energy-dependent transfer times $\tau(E)$, using the energetic stabilization of the excess electrons as a measure of their degree of solvation. As the spectral feature of the solvated electrons, e_S, is due to the amorphous environment an inhomogeneously broadened distribution, i.e. e_S exhibits a finite spectral width, the question arises whether the observed shift of the peak maximum, Σ_S (cf. Fig. 4.02), represents the energetic stabilization σ_S of the solvated electrons. Assuming energy-dependent transfer times $\tau(E)$, the electrons contributing to the e_S distribution will have different transfer probabilities. The faster decay of the energetically higher lying electrons may lead to an *apparently* faster energetic shift of the peak maximum. In the following, a simple empirical model based on rate equations for electron transfer and solvation will be introduced. It includes energy-dependent transfer times $\tau(E)$ and a constant stabilization rate σ_S and therefore the competition of charge transfer and solvation at ice-metal interfaces.

Empirical Model Description: The solvated electron population at a certain time t after photoinjection shall be denoted by $N(t,E)$. Following the above discussion, the number of electrons at the energy E (i) *decreases* due to back transfer to the substrate with a rate $\tau^{-1}(E)$ and the subsequent stabilization to lower energies $E - \delta E$ with the constant rate σ_S. At the same time, the population (ii) *increases*, because electrons from higher lying energies $E + \delta E$ stabilize while having the back transfer probability $\tau^{-1}(E + \delta E)$. The electron population changes with time according to

$$\frac{\partial N(t,E)}{\partial t} = \underbrace{-\left(\sigma_S + \frac{1}{\tau(E)}\right) \cdot N(t,E)}_{i} + \underbrace{\left(\sigma_S - \frac{1}{\tau(E+\delta E)}\right) \cdot N(t, E + \delta E)}_{ii} \qquad (4.1)$$

where the first term (i) denotes the population *decrease* and the second (ii) describes the *increase*. To account for the two regimes of charge transfer, substrate-dominated and barrier-determined, the transfer time was assumed to be $\tau_0 = $ *const.* for energies above the barrier maximum ($E_{barrier}$) and exponentially energy-dependent for $E \leq E_{barrier}$:

$$\tau(E) = \begin{cases} \tau_0 & for \quad E_{barrier} < E \\ \tau_0 \cdot \exp[\gamma \cdot (E_{barrier} - E)] & for \quad E_{barrier} \geq E \end{cases} \qquad (4.2)$$

In this sense, τ_0 reflects the influence of the surface electronic band structure of the substrate (including all elastic and inelastic components). The exponential increase of the transfer time with energetic stabilization approximates the complex evolution of the "real" barrier that becomes broader and higher with ongoing solvation (Fig. 4.05, left). If equation (4.2) is brought into the form of the tunneling probability of a rectangular barrier

$$\tau^{-1}(E) = \tau_0^{-1} \cdot \exp\left[-\frac{2d}{\hbar} \sqrt{2m \cdot (E_{barrier} - E)} \right] , \qquad (4.3)$$

a series of rectangular barriers with the effective width

$$d_{eff}(E) = \gamma \cdot \left(\frac{\hbar}{2}\right) \sqrt{\frac{E_{barrier} - E}{2m}} \qquad (4.4)$$

results. Due to the square root, this expression is similar to the width increase of a parabola as a function of height (green curve in Fig. 4.05). The exponential increase of the transfer times with ongoing stabilization in equation (4.2) can therefore be interpreted as the following: The transfer probability through the *real* barrier corresponds to the transition probability through an *effective* rectangular barrier. The complex evolution of the real barrier is approximated by a series of rectangular barriers, which has the same width dependence as a parabola.
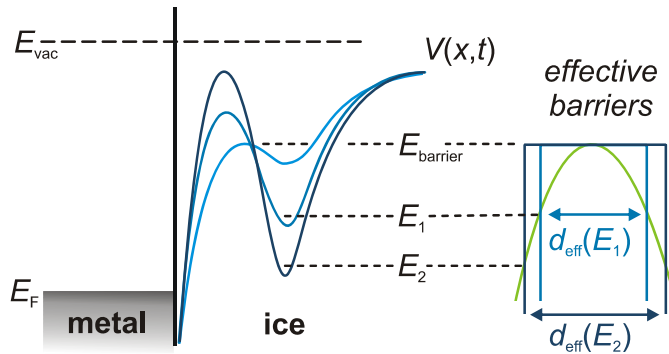

Fig. **4.05:** *Real and Effective Barriers.* The complex evolution of the real interfacial barrier is approximated by a series of rectangular barriers with effective widths. See text for details.

Despite these rather simplistic assumptions, the presented model reproduces the data almost perfectly as shown in Fig. 4.06. Using barrier heights $E_{barrier}$ = 2.77 eV (D$_2$O/Ru(001)) and 2.93 eV (D$_2$O/Cu(111)) and substrate-determined transfer times τ_0^{Ru} = 20 fs and τ_0^{Cu} = 67 fs, both regimes of charge transfer for both employed substrates are excellently reproduced (Fig. 4.06, bottom).[67] Note, that τ_0 cannot simply be set equal to the initial transfer times τ_1 obtained from the simple exponential fit; while the exponential fit gives an average value for the charge transfer time in the fitted time interval, τ_0 stands for the bare transfer probability if there were *no* barrier.

In addition to the population dynamics, the transient peak shift of e$_S$ was also simulated according to rate equation (4.1). To achieve the excellent agreement of data and model calculation for both dynamical features of the solvated electrons, i.e. peak shift *and* population decay (cf. Fig. 4.06), similar stabilization rates σ_S for both systems, D$_2$O/Ru(001) and D$_2$O/Cu(111), had to be used: σ_S^{Ru} = 0.24 eV/ps and σ_S^{Cu} = 0.22 eV/ps.

---

[67] An initial Gaussian energy distribution with the width of 80 meV was employed for the fit around 2.8 and 2.9 eV for Ru(001) and Cu(111), respectively. To account for the finite duration of the laser pulses the resulting transients were convolved with the pulses envelope, similar to the procedure employed for the exponential fits.

Apparently, the constant rate of stabilization is similar for both substrates although the observed peak shift Σ_S differs *significantly* for the $D_2O/Cu(111)$ and $Ru(001)$ system. Hence, the simple model description of the electron dynamics at the ice-metal interfaces shows that a significant contribution of the energetic shift of the peak maximum at the ice-Ru interface Σ_S^{Ru} results from the energy dependent transfer time $\tau^{Ru}(E)$. As τ_0^{Ru} is significantly larger than τ_0^{Cu}, the effect of different transfer times within the energetic distribution of solvated electrons is much larger for $D_2O/Ru(001)$ than for $D_2O/Cu(111)$. Thus, the observed difference between Σ_S^{Ru} and Σ_S^{Cu} can be ascribed to an *apparent* peak shift introduced by the energy-dependent transfer rates. Hence, the interpretation of observed peak shifts as a quantitative measure for electron stabilization has to be treated with caution if systems with varying transfer times are investigated. Moreover, the similarity of σ_S^{Ru} and σ_S^{Cu}, i.e. the similar stabilization in both adlayers, corroborates that the local environment of the solvated electrons, the solvation shell, is hardly affected by the underlying substrate. The different water-metal interaction of the first layer D_2O on the two substrates (cf. 2.4.3) apparently does not affect the solvation shell.
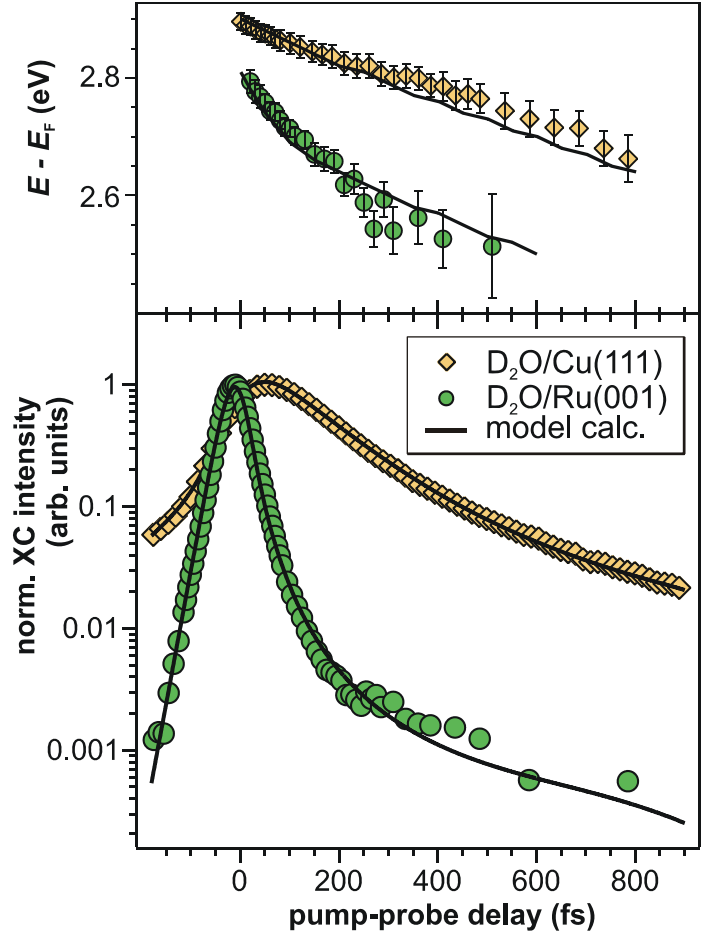

Fig. 4.06: *Best Fit of Empirical Model.* The rate equation model reproduces both, energy- (top) and time-dependent data (bottom), for $D_2O/Cu(111)$ and $Ru(001)$ using similar stabilization rates σ_S for both substrates. See text for details.

The pre-exponential factor γ in equation (4.2) can be interpreted as a measure for the relation between the effective barrier thicknesses for the $D_2O/Cu(111)$ and $Ru(001)$ system at a fixed $E_{barrier} - E$, because it also enters equation (4.4) for the effective barrier widths. From the fitting of the data, a γ^{Ru} twice as large as γ^{Cu} results. In other words, the barrier at the ice-Ru interface is effectively twice as wide at any energy as for $D_2O/Cu(111)$.[68] This result is

---

[68] The effective widths resulting from equation (4.4) are on the order of several angstrœms: $d_{eff}^{Cu}(0.1eV) = 1.8$ Å, $d_{eff}^{Ru}(0.1eV) = 3.6$ Å, $d_{eff}^{Cu}(0.3eV) = 3.2$ Å, and $d_{eff}^{Ru}(0.3eV) = 6.4$ Å. However, in reality the solvated electron does *not* move further outwards with ongoing solvation.

reasonable, as for the first bilayer of D_2O/Ru(001) no electron solvation is encountered. [Gah04] The strongly-bound first bilayer therefore acts as an additional spacer layer and thus increases the width of the tunneling barrier, i.e. keeps the electrons further away from the metal surface.

Although the model description used is conceivably simple, it reproduces peak shift and population dynamics for both systems remarkably well. A quantitative interpretation of the employed parameters should be treated carefully, however. Nevertheless, it is noteworthy that the ratio of the transfer times, which reflects the overall influence of the substrate electronic band structure on the electron dynamics, $\tau_0^{Cu}/\tau_0^{Ru} = 3.3$, agrees quite well with the ratio of the band gap widths $\Delta k_{gap}^{Cu} / \Delta k_{gap}^{Ru} = 3.2$. This would mean that the electron back transfer is mainly mediated by *elastic* back relaxation, which is reasonable as a localized, solvated electron does not interact with many scattering partners. In addition, a linear dependence of charge transfer time on the required momentum change would result.

In summary, a dynamical transition between the substrate-dominated and the barrier-determined transfer regimes has been observed. While at early times, right after photoinjection ($t < 300$ fs), the electron transfer is influenced considerably by the substrate, the enhanced screening at later delays leads to a decreased overlap of the solvated electron wave function with metal states. The tunneling through an interfacial barrier becomes the rate-limiting step for electron back relaxation. As shown by a simple empirical model calculation, the stabilization rate σ_S is similar for both substrates. It can be concluded that the solvation shell of the excess electron in ice layers on Ru(001) and on Cu(111) does not differ significantly. Accordingly, the next paragraph is devoted to the influence of the ice structure on the electron transfer and solvation dynamics, aiming at a more complete understanding of the involved fundamental processes.

4.1.2 Impact of the Ice Structure

As the solvated electron has a localized character, microscopic characterization of its environment is crucial for a deeper understanding of involved fundamental processes. The electron's energetic stabilization and screening from the metal substrate results from its direct interaction with the surrounding solvent molecules – the influence of the local structure on these dynamics lies at hand. Investigation of the impact of ice structure on electron dynamics at ice-metal interfaces accordingly requires a probe of the ice structure on a molecular level. A powerful technique to investigate structure with sub-nanometer resolution in real space is scanning tunneling microscopy (STM). A collaboration with K. Morgenstern and M. Mehlhorn at the University of Hanover, who are experts in low-temperature STM of water on metal surfaces, [Mor02a, Mor02b, Meh05] was established. This cooperation made the investigation of amorphous D_2O *clusters* deposited onto the Cu(111) surface by low-temperature STM *and* time-resolved 2PPE spectroscopy possible. By combining these two complementary techniques, a real-space and a time-resolved method, the correlation of ice cluster morphology and electron dynamics is revealed.
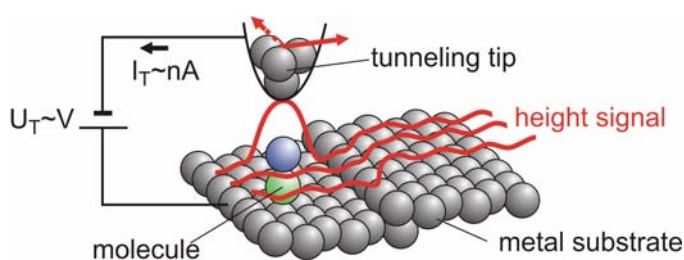
Fig. 4.07: *STM Scheme.* A bias voltage enables electron tunneling between tip and sample. A distance dependent tunneling current flows between them that yields information about the local electronic structure of the sample. The scheme depicts the *constant-current* mode (adopted from [Meh05]).

The ice clusters are imaged using a custom-built low-temperature STM. Its excellent design makes imaging at 5 K possible, which is a necessary condition for the sub-pA stability of the apparatus. Details on the STM setup and measurement technique can be found elsewhere. [Meh05, Meh07] The principle of measurement can be summarized as follows: A nanoscale, metallic tip is positioned a few Ångstrœm over an adsorbate-covered, conductive surface (Fig. 4.07). Due to the applied bias voltage on the order of 1 eV and the small distance the electronic wave functions of the tip and the sample overlap, a tunneling current flows, which depends on the applied voltage and the tip-sample distance. This current depends exponentially on the voltage and distance and contains information about the character and spatial distribution of the electronic states of the sample. Imaging of a sample is either done in *constant-height* or *constant-current* mode: In the former case the tip-sample distance is fixed during scanning and the tunneling current is recorded. In the second mode, which is most often used, the current is kept constant while distance is controlled via a feed-back loop. Thus, the tip roughly follows the corrugation of the surface and the height signal gives a nearly topological image.[69]

It is difficult to perform STM measurements on water clusters, since ice is an insulator with a wide band gap: If the applied bias voltage leads to tunneling through the ice band gap, the apparent height of the clusters, deduced from the height signal above the clusters, underestimates the real height. As the tip-metal distance has to be larger than the real height of the clusters in order to avoid mechanical manipulation, the ability to detect tunneling currents down to few pA is necessary. If, in contrast, the applied bias voltage leads to tunneling through the ice conduction band, the conductivity becomes comparable to the bare metal surface.[70] The apparent height of the clusters is in this case close to the real height.
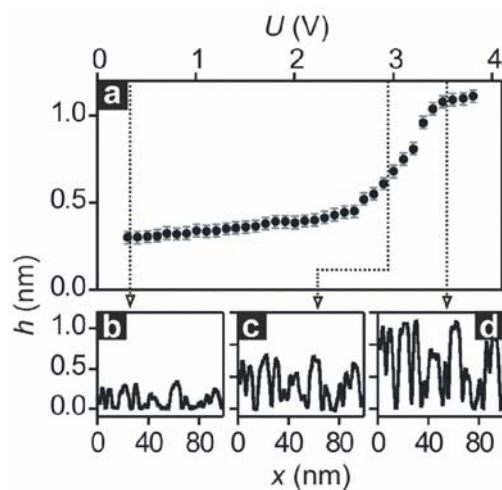
Fig. 4.08: *Apparent Height.* Depending on the tunneling voltage the measured height is underestimated due to tunneling through the ice band gap. See text for details (adopted from [Stä07]).

---

[69] To achieve high spatial resolution, piezoelectric crystals are employed for tip positioning.
[70] This happens due to strong coupling of the molecular orbitals to emptiy metal states.

However, tunneling through the conduction band increases the probability of electron-induced modifications of the ice clusters. [Mor02b] Fig. 4.08a shows the height dependence on the bias voltage at a constant current of 500 fA for amorphous D_2O clusters on Cu(111). The panels (b) – (d) depict line scans of the sample at bias voltages indicated by the dotted arrows. At low voltages (b) tunneling occurs through the band gap and the height $h = 0.3$ nm underestimates the real height of the clusters. Only weak variations of h are encountered until the onset of the conduction band is reached. The apparent height increases for $U > 2.7$ eV (Fig. 4.08c) and saturates for bias voltages above 3.5 eV (Fig. 4.08d). As discussed above, the measured height $h = 1.1$ nm (for the higher voltages) approximates here the real geometric height, as tunneling occurs across the ice conduction band.

Fig. 4.09 shows STM images of D_2O clusters on the Cu(111) surface. The nominal coverage of D_2O corresponds to 1 BL. The ice clusters depicted in Fig. 4.09A were dosed at 85(3) K. Their size distribution is narrow and the clusters exhibit no defined shape in any direction. Due to their lack of long- and short-range order the clusters are amorphous, which is in agreement with current understanding. [Ste99] Annealing of the as-dosed clusters for 2 s to 120(3) K leads to changes at the D_2O/Cu(111) interface (cf. Fig. 4.09B). Although the onset of D_2O desorption from the Cu template lies at significantly higher temperatures (~150 K, see 3.3.2 and [Gah04]), less metal surface area is covered by D_2O after annealing. In addition, the size distribution broadens. Scans along the dark and light blue line in panel A and B, respectively, show that also the cluster height decreases after annealing. (Fig. 4.09C) However, the high-resolution image (inset of panel B) confirms that the clusters are still disordered and therefore also amorphous. The heating is governed by a significant decrease of cluster volume: Integration of the cluster volume before and after annealing shows that the volume is reduced substantially by 40(8) %.[71] As desorption is not observed at 120 K,[72] this enormous reduction
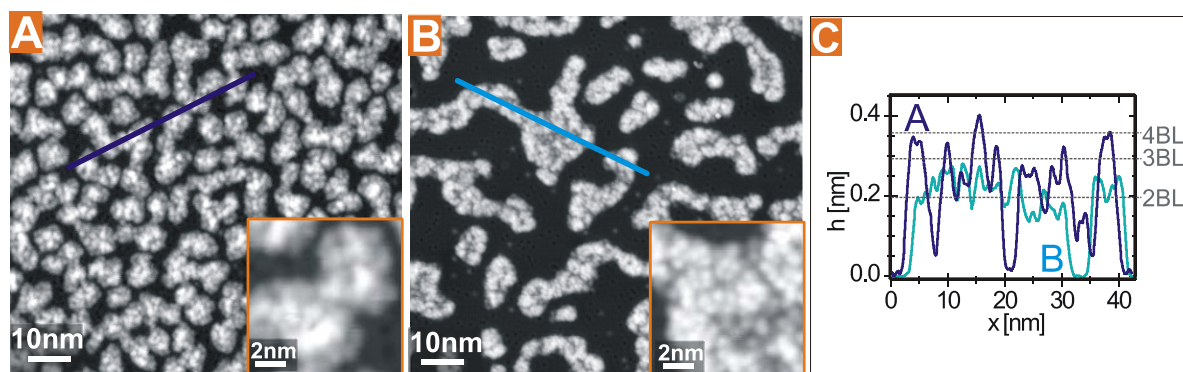

Fig. 4.09: *STM Images of Porous and Compact Amorphous Ice Clusters on Cu(111).* (A, B) STM images of amorphous D_2O/Cu(111) (nominal coverage: 1 BL) as deposited at 85 K (A; 0.2 V, 1 pA) and after annealing at 120 K (B; 0.1 V, 9 pA). The high resolution images (insets) show that both structures are disordered, i.e. amorphous. (C) The line scans in (A, B) lead to the apparent height h distribution as depicted (left axis). The right axis gives the corresponding real height (modified from [Stä07]).

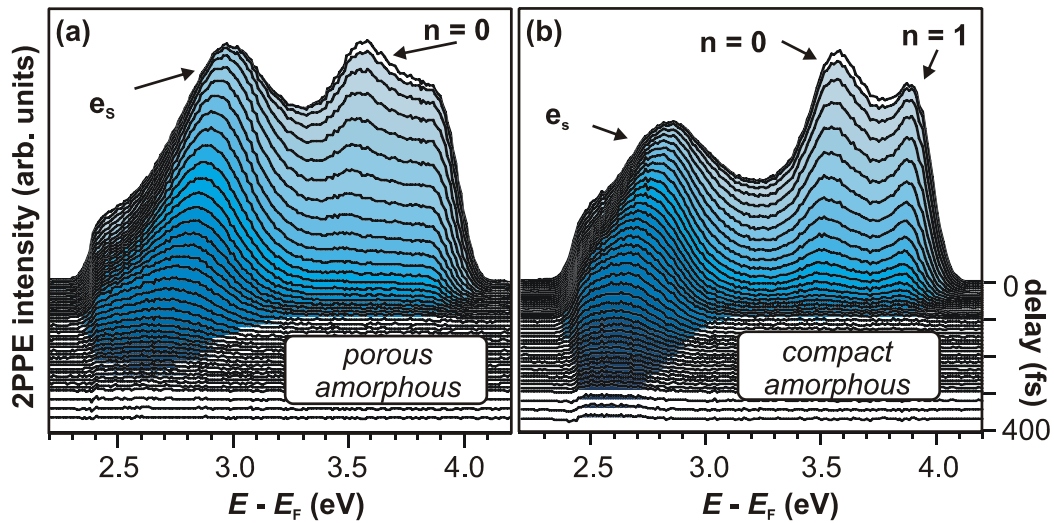[71] The real, geometrical height was used for integration.

Fig. **4.10**: *2PPE Data of Porous and Compact Amorphous Ice Clusters.* Besides the spectral signature of the solvated electrons ($h\nu_1$ = 3.99 eV, $h\nu_2$ = 2.04 eV), the spectra also exhibit contributions of the Cu(111) surface (n=0) and image potential state (n = 1). The e_S peak maximum lies for the compact clusters (b) lower in energy at t = 0 than for porous ice.

of the cluster volume can only be attributed to the existence of pores in the as-dosed clusters, which collapse upon annealing. Hence, the as-deposited clusters will be termed *porous amorphous* and the annealed structure *compact amorphous* in the following.

Fig. 4.10 depicts time-resolved (right axis) 2PPE data for clusters grown under conditions nominally identical to the STM study, i.e. sample temperatures of 85(3) K (Fig. 4.10a) and 120(3) K (Fig. 4.10b).[73] As the Cu(111) surface is not completely covered by ice,[74] the spectra exhibit also significant contributions from the metal substrate. The peak at $E - E_F$ = 3.6 eV, which appears in both data sets, results from the occupied Cu(111) surface state (n = 0, cf. 2.4.2). In addition, a distinct peak below $E - E_F$ = 3 eV is observed. It exhibits a finite lifetime to positive delays, i.e. is excited by UV photons and probed by visible light. Additionally, the maximum of this peak shifts down to lower energies with increasing time delay. This agrees with the investigation of the amorphous ice multilayer of D_2O/Cu(111) assigned to solvated electrons in the ice, which are stabilized and screened by the surrounding polar molecules (cf. 4.1.1). As the spectral signature e_S is encountered for both morphologies, porous and compact amorphous ice (Fig. 4.10a and b, respectively) it can be concluded that electron solvate in both types of amorphous ice clusters on Cu(111).

D_2O clusters adsorbed on the Cu(111) surface exhibit three further types of structures upon crystallization, in addition to porous and compact amorphous ice. Those were also found in collaboration with K. Morgenstern and M. Mehlhorn. [Meh05, Meh06] Thus, before turning to a quantitative analysis of the 2PPE data shown above, these structures will be introduced in the

---

[72] The onset of measurable D_2O desorption starts at ~150 K.

[73] The sample temperature during measurement is 25 K, the nominal coverage adds up to 0.8 BL.

[74] For comparison with a completely wetted Cu(111) surface see Fig. 2.09.

following. Fig. 4.11 summarizes all observed ice structures of D_2O/Cu(111) as a function of annealing temperature. After D_2O deposition at 90 K, the ice clusters experience three metastable phases upon heating before they fully crystallize. [Meh05]. As discussed above, D_2O deposition at 85 K leads to porous amorphous ice clusters, and annealing to 120 K results in the familiar transition to compact amorphous clusters. In addition to these two morphologies of amorphous ice, well-ordered structures of D_2O/Cu(111) occur when annealing the sample to higher temperatures: At 130 K a striped faceting is observed. The D_2O arranges in a local (2×1) structure and forms islands of 1.18(2) nm height corresponding to 3.5 BL. The facets develope on top of a 2 BL thick base layer. [Meh05] Despite the periodic character of these *facetted clusters* the observed structure is metastable. Further annealing to 145 K leads to the formation of pyramidal islands on top of the 2 BL base layer as depicted in Fig. 4.11. The triangular, obtuse pyramids exhibit heights of 2-3 BL. Completely crystallized D_2O clusters are achieved by heating to the onset of D_2O desorption, to 148 K. Crystallites form, which consist of a 5 BL thick base layer, on top of which 2-3 BL high pyramidal islands occur. A detailed analysis of theses structures can be found in [Meh05].
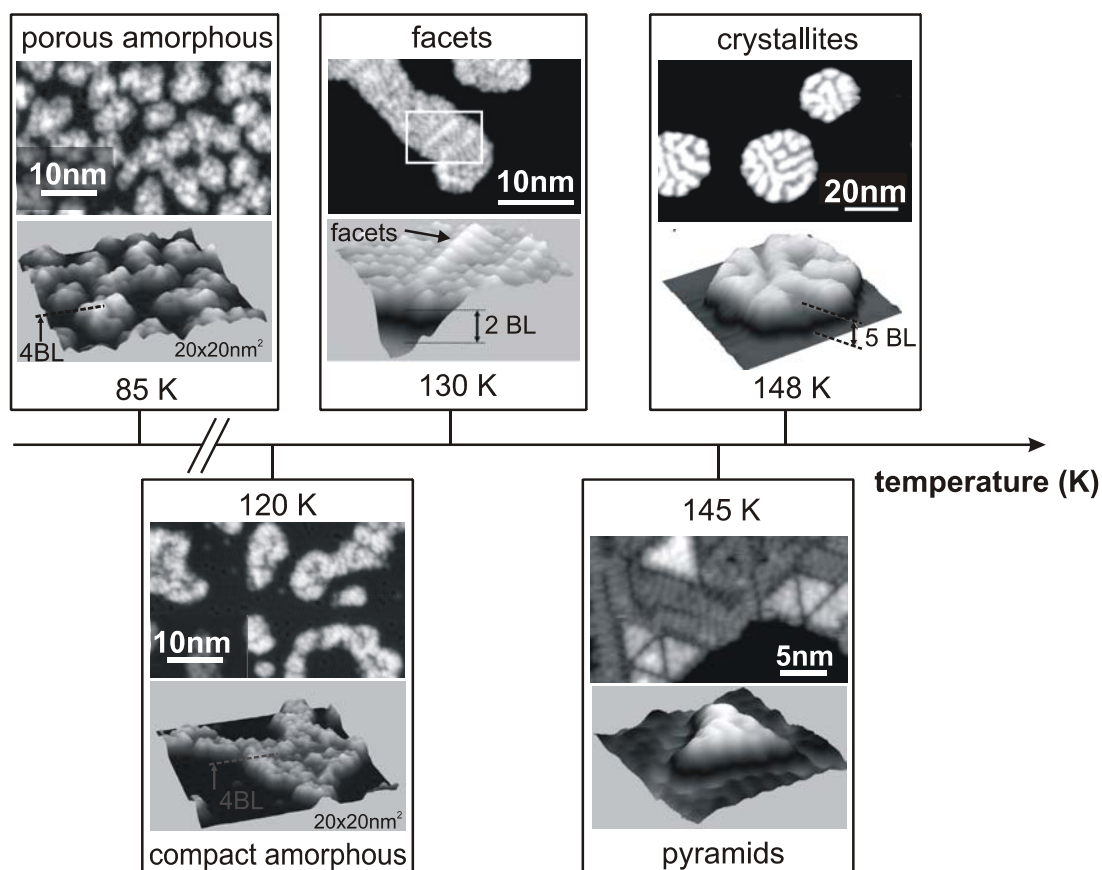

Fig. 4.11: *Stable and Metastable Structures of D_2O/Cu(111).* The crystallization of amorphous ice clusters occurs via four metastable structures. Besides the porous (90 K) and compact amorphous ice (120 K), facetted islands are observed upon annealing for 15 min to 130 K. Heating to 145 K (15 min) leads to the formation of pyramidal islands on top of a 2 BL high base layer. Finally, the stable crystalline structure is reached by annealing the sample to 148 K for 2 s. Crystallites of 8 BL height form. They consist of a 5 BL high base layer on top of which 2-3 BL high pyramids are observed (modified from [Meh05]).

It is apparent from Fig. 4.11 that the structure of the supported ice clusters varies significantly upon crystallization. Hence, a comparison of this structural data with time-resolved 2PPE measurements of these systems can lead to interesting insight. 2PPE experiments were performed under nominally identical conditions as for the STM study. Fig. 4.12a depicts the shift of the peak maximum[75] of the solvated electron distribution as a function of pump-probe time delay for *porous amorphous* (triangles), *compact amorphous* (diamonds), *facetted* (circles), and *pyramidal clusters* (squares).[76] For compact clusters, the peak maximum of e_S lies 140 meV lower in energy than for the porous ice ($t <$ 100 fs). Linear fits to the data (black lines) give a considerably faster shift of Σ_S^P = -2.0(1) eV/ps for the porous clusters compared with the compact ones (Σ_S^C = -1.3(1) eV/ps). For delays larger than $t >$ 150 fs the 2PPE intensity becomes quite low and the e_S distribution approximates the low-energy cut-off (cf. Fig. 4.10). Therefore, the error bars of the peak shifts become very large at these time delays. Nevertheless, it is apparent from Fig. 4.12a that the energetic shift of the e_S peak maximum changes significantly upon the transition from porous amorphous to compact clusters.

As discussed for Fig. 4.11, the structural transition from compact ice to the facetted and pyramidal clusters is far more dramatic than the porous-compact transition, as the D_2O starts to assemble periodically. However, the peak shift of e_S is affected by this transition to a small degree only: The datasets for the ordered ice (circles and squares) coincide with the compact cluster peak shift within the experimental resolution.
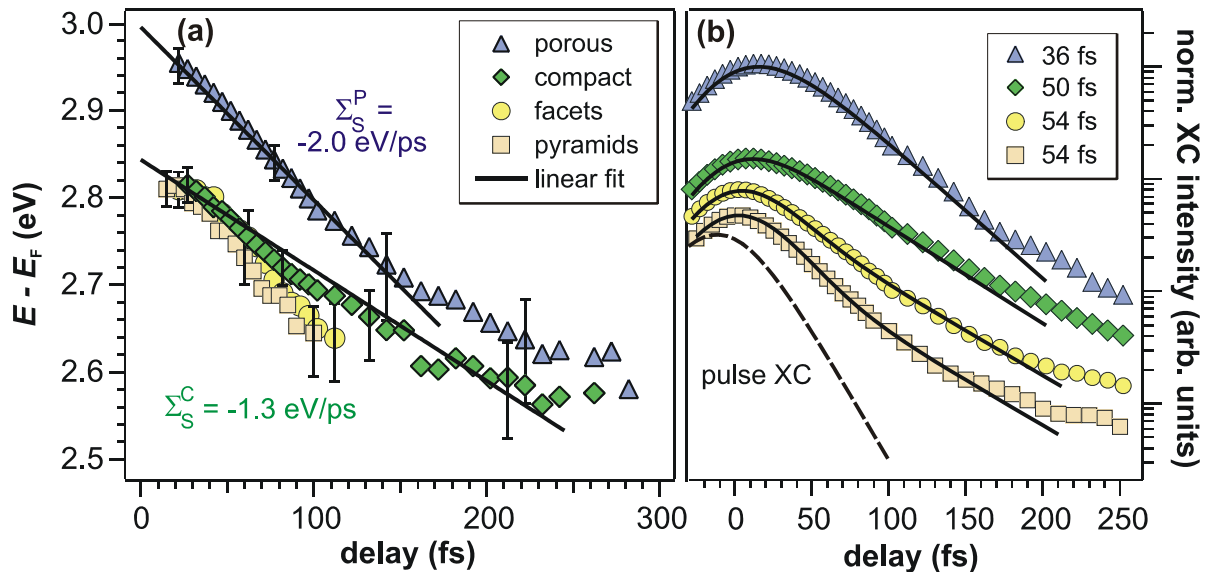

Fig. 4.12: *Data Analysis for Porous, Compact, Facetted, and Pyramidal Clusters.* Electron Dynamics decelerate upon the transition to compact ice, but hardly change for the subsequent structural transitions. a) Time-dependent shift of the peak maxima and linear fit to the data. b) Population decay traces and single-exponential fits. Traces are vertically shifted to ensure visibility. See text for details.

[75] As for the D_2O multilayers (cf. 4.1.1) the peak maxima were determined manually due to the strong and time-dependent background.
[76] The 2PPE data of crystallites is not shown, as the electron solvation dynamics in crystalline ice will be discussed in section 4.2.

Fig. 4.12b shows XC traces of the solvated electron population for the investigated structures. As can be seen from the data, the electron back decay to the metal substrate changes upon the transition from porous to compact clusters. Single exponential functions were convolved with the laser pulse envelope and fitted to the traces. The resulting least square fits are represented by the black curves and give initial decay times of $\tau^P = 36(5)$ fs for the porous ice and $\tau^C = 50(5)$ fs for the compact clusters. Apparently, the electron transfer dynamics decelerate considerably by 30% upon the structural transition. However, the transition to the well-ordered facetted and pyramidal islands does not change the electron population dynamics significantly. The single exponential fits result in initial decay times of 54(5) fs for both, facetted and pyramidal ice. Apparently, the lifetime of the solvated electrons remains, within the experimental resolution, unaffected by the transition from amorphous to ordered ice. In other words, neither the peak shift, nor the screening of the excess electron by the water molecules is altered by the significant modifications of the structures observed by STM (cf. Fig. 4.11).

As the transition from porous to compact amorphous ice changes the electron dynamics much more significantly than the one to facetted and pyramidal ice, the following detailed analysis will focus on the two amorphous types of clusters. The discussion of the similarity of the electron dynamics in compact, facetted, and pyramidal ice *despite* the dramatic structural changes observed by STM is highly important and will be resumed in paragraph 4.1.3.

It was shown in paragraph 4.1.1 for the electron transfer and solvation dynamics in ice *multilayers* that peak shift and population dynamics are strongly connected to each other. A mere comparison and interpretation of the above derived fit parameters must therefore be treated carefully. In addition, all linear and exponential least square fits shown in Fig. 4.12 (dashed lines) show only poor agreement with the data. Hence, to facilitate conclusions, the empirical rate equation model derived in paragraph 4.1.1 is applied to the cluster data. The main idea of this approach is, as mentioned before, the implementation of the transient barrier, which evolves due to the subsequent screening of the excess charge, by a series of effective rectangular barriers with constant heights E_{barrier} that approximate the energy-dependent transfer times $\tau(E)$. The parameter γ in

$$\tau(E) = \tau_0 \cdot \exp[\gamma \cdot (E_{barrier} - E)] \qquad \text{for} \qquad E < E_{\text{barrier}} \qquad (4.5)$$

is a measure for the *screening efficiency* of the system: The larger it is, the more pronounced is the increase of transfer time with increasing binding energy, i.e. solvation. Using constant stabilization rates σ_S, this approach connects the time-dependent peak shift of the solvated electrons with the transient population decay. Fig. 4.13 depicts peak shifts (top, right axis) and population transients (bottom, left axis) of porous and compact amorphous ice clusters. The black curves are the least square fits of the empirical model to the cluster data. All datasets, peak shift *and* population decay for porous *and* compact clusters are reproduced very well. Table 4.01 summarizes the fit parameters used and compares them with the multilayer $D_2O/Cu(111)$ discussed in paragraph 4.1.1.

The stabilization rate σ_S, initial decay time τ_0, *and* the energy difference $\Delta E = E_{\text{barrier}} - E_0$ between barrier maximum and e_S distribution maximum at $t = 0$ are similar for both types of
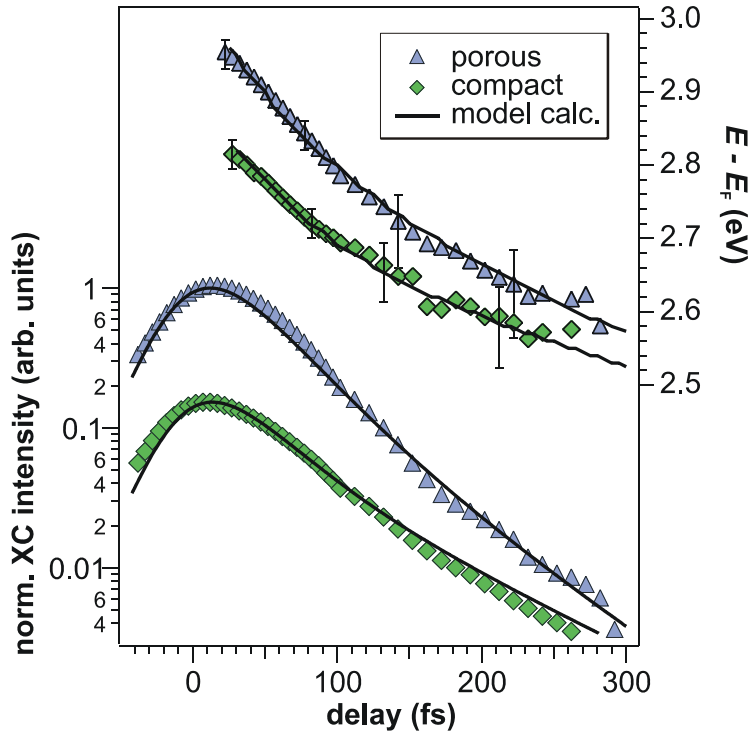
Fig. 4.13: *Empirical Model for Porous and Compact Clusters.* Both, time-dependent peak shift of e_S (top, right axis) and the population decay (bottom, left axis) are excellently reproduced by the empirical model (black curves).

clusters. ΔE and τ_0 describe the degree of screening encountered by the excess electrons right after photoinjection: While τ_0 is a measure for the pure coupling degree of the electron to the metal substrate, ΔE expresses the influence of the solvent screening *before* enhanced screening due to further solvation occurs. The coincidence of these parameters for porous and compact clusters therefore shows that the initial screening of the solvated electrons is similar for both types of clusters although the decay time increases by 30% upon the structural transition. In addition, the model calculation shows that the stabilization rate σ_S is similar for porous and compact clusters. The energetic stabilization due to the reorientation of the water molecules is not affected by the structural transition although the binding energy after injection and the peak shift of the two cluster types differ.

	porous	compact	multilayer
σ_S (eV/ps)	0.22	0.22	0.22
τ_0 (fs)	25	25	67
$E_{barrier}-E_0$ (meV)	-20	-20	+30
$\gamma\,(\gamma^{ML})$	0.45	0.8	1

Tab. 4.01: *Fit Parameters for the D_2O Multilayer, Porous, and Compact Clusters.*

The only difference in parameters for the porous and the compact clusters is the pre-exponential factor γ. As apparent from equation (4.5), this quantity describes the increase of decay time with ongoing solvation and is – as mentioned before – a measure for the screening

efficiency of the investigated sample. The structural transition from porous to compact ice leads to a doubling of this value, showing (i) that the screening of the water molecules in the porous clusters is half as efficient as in the compact ice and (ii) that the significant changes of peak shift and population decay upon the structural transitions result *only* from the screening efficiency: The slower population decay of the compact clusters originates from the more efficient reaction of the screening solvent molecules, and the slower peak shift is – as in the multilayer case – due to different energy-dependent transfer times $\tau(E)$.

Quantitative comparison of these fit parameters to the multilayer of D_2O on Cu(111) reveals the changes of electron dynamics due to clusterwise growth. The stabilization rate σ_S is similar for all types of D_2O on the Cu(111) surface (and also on the Ru(001) substrate). This means that the reaction of the surrounding water molecules leads to a similar energetic stabilization of the excess charge regardless of the different adsorption type. However, the parameters τ_0 and ΔE, describing the initial conditions after photoinjection, are different for clusters and layers: The initial decay time τ_0 is larger for the D_2O multilayer, i.e. the initial coupling to metal states is lower. The relative influence of the solvent, described by ΔE, is larger for the closed ice layers. Apparently, the higher number of molecules in the multilayer leads to a stronger initial screening of the excess electron. In addition, also the screening efficiency γ, which describes the dynamic response of the water molecules on the electron, is larger for the ice layers compared with both types of clusters. In other words, starting with electrons that are already more efficiently screened, the transient decoupling of the excess charge is also more efficient in the ice multilayer.

However, reliable interpretation of the above results requires knowledge of the binding site of the solvated electrons. Depending on the character of the solvated electron, bulk- or surface-bound, the similarities and differences of the initial starting conditions (ΔE and τ_0) and the dynamic response of the solvent (σ_S and γ) would lead to different consequences. Therefore, the binding site of the solvated electrons will be addressed to in the following paragraph, including a detailed discussion of the parameters derived above.

4.1.3 Surface vs. Bulk Solvation

Having shown that the ice morphology has considerable impact on the electron solvation dynamics for the porous-compact transition, knowledge of the binding site of the excess electrons is required. Hence, the present paragraph will first reveal the binding character of the hydrated electrons at ice-metal interfaces before turning to a discussion of the model calculation analysis derived above. This discussion will be separated into four parts: (i) Comparison of porous and compact ice clusters, (ii) association of these results with the ice multilayer, (iii) incorporation of the results for the facetted and pyramidal clusters, and (iv) conclusions concerning the controversial surface-bulk debate of the gas phase ice clusters.

Solvation Site: As mentioned in section 2.2, there is a long-standing debate about the binding character of solvated electrons in water anion clusters in the gas phase. Different isomers, each of them attributed to solvated electrons, were found by experiment [Coe90, Ver05a, Coe06] and theory [Bar88, Tur05a]. Although it is agreed that *there is* a surface to bulk transition of the solvated electron species as a function of cluster size, the cluster size range, where this transition occurs, is still under discussion.

The surface science approach employed in the present work allows for the determination of the excess electron's solvation site at the ice-metal interfaces by adsorption of a xenon adlayer on top of the adsorbed ice clusters or layers as depicted in Fig. 4.14. If the solvated electrons would reside at the (former) ice-vacuum interface, significant changes in the photoelectron spectra would be expected: The direct interaction with the charge cloud would significantly polarize
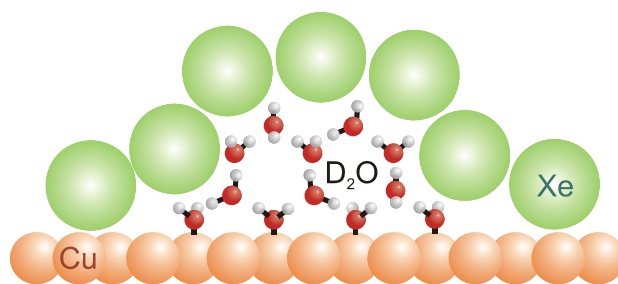

Fig. 4.14: *Xe Overlayer Experiment.* Due to the differing interaction of bulk- and surface-bound solvated electrons with the rare gas atoms the solvation site can be determined.

the rare gas atoms, and the xenon atoms would constrict ("squeeze") the wave function of the solvated electrons. However, if the hydrated electrons solvate in the bulk of the ice clusters or layers, no significant changes in the photoelectron spectra are expected, as only the net electric field of the screened solvated electron could polarize the Xe, which would cause – if at all – only slight changes of the electron dynamics.

Porous and compact amorphous ice clusters were prepared using the above described procedures. Cooling the sample down to 25 K enables the adsorption of Xe atoms on top of the $D_2O/Cu(111)$ interface.[77] Fig. 4.15a depicts 2PPE spectra of the Cu(111) substrate covered with compact ice clusters before (black) and after adsorption of 2 ML Xe (grey).[78] The energetic shift of the solvated electron feature e_S^I by more than 400 meV is easily recognized. The work function change (shift of the secondary edge) is, with 40 meV, clearly smaller than the peak shift of e_S, which confirms that the spectral change is due to the interaction of the solvated electrons with the rare gas atoms and does *not* result from the potential energy change at the interfaces upon Xe adsorption only.[79] The enormous shift of the peak maximum of the solvated electron distribution can be continuously monitored as a function of Xe exposure as depicted in Fig. 4.15b. The overlayer experiment was performed for *both* types of amorphous clusters, porous (diamonds) and compact (triangles), showing that the peak shifts continuously

---

[77] Xenon desorbs from metal surfaces for temperatures > 50 K.

[78] The Xe coverage was calibrated on the bare Cu(111) surface.

[79] The position of the $n = 0$ surface state of the Cu(111) surface does not change upon Xe adsorption. The $n = 1$ image potential state of the bare Cu(111) is pinned to the local workfunction (4.95 eV) with a binding energy of 0.8 eV. Therefore, its signal overlaps with the surface state signature for the $D_2O/Cu(111)$ system. In agreement with literature [Wol96] the IPS shifts upon Xe exposure closer to the Fermi Level mainly due to the Xe-induced work function change of the formely bare Cu patches.
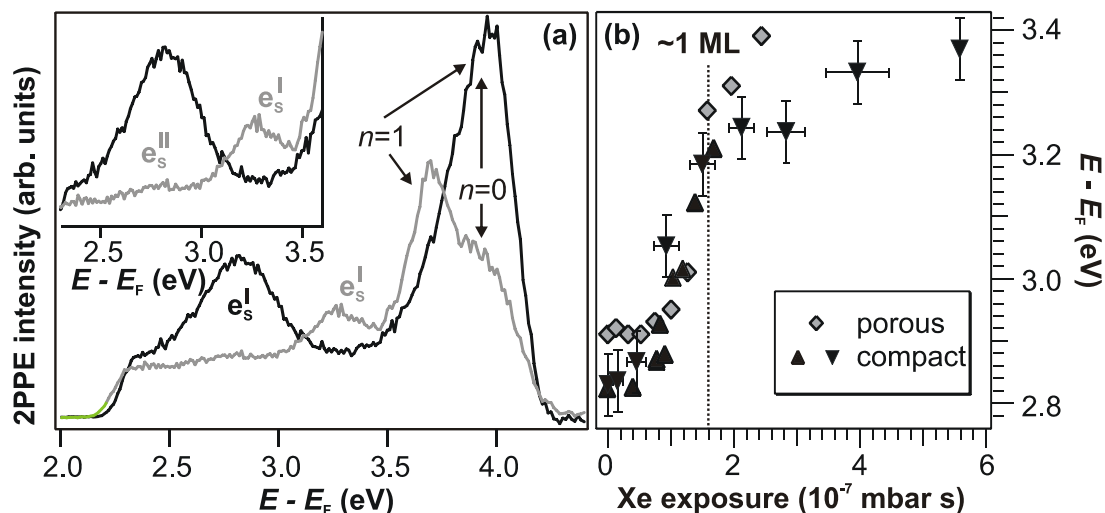
Fig. 4.15: *Influence of the Xe Adlayer.* a) 2PPE spectra of compact clusters before (black) and after adsorption of 2 ML of xenon (grey). b) Continuous shift of the solvated electron distribution upon Xe exposure.

by more than 400 meV to higher energies with respect to the Fermi Level, regardless of the morphology of the ice clusters. The dramatic change of the solvated electrons' binding energy upon Xe exposure thus unambiguously shows that the excess electrons interact *directly* with the Xe atom, i.e. that they bind at the surface of the ice clusters. However, the inset of Fig. 4.15a shows that a small fraction of the solvated electron distribution e_S^{II} is not affected by the Xe atoms. They stem from sites that are not titrated with rare gas atoms.

The significance of the enormous shift of e_S^I becomes apparent when comparing the spectra to the same experiment for the wetting layer of $D_2O/Cu(111)$. Fig.4.16 shows 2PPE spectra of a 4 BL compact amorphous *multilayer* of $D_2O/Cu(111)$ before (black) and after titration with 2 ML of xenon (grey). The peak of the solvated electron distribution does not shift upon Xe adsorption for the ice multilayer case. This means that for wetting multilayers, the solvated electrons reside in the bulk of the ice film. Their electric field is more efficiently screened from the rare gas atoms so that the polarizability of the xenon cannot change the binding energy of the solvated electrons.

Porous and Compact Clusters: Having identified the binding site of the hydrated electrons for D_2O clusters and the wetting layer on the Cu(111) surface, the differences of the electron dynamics in porous and compact amorphous ice clusters can be
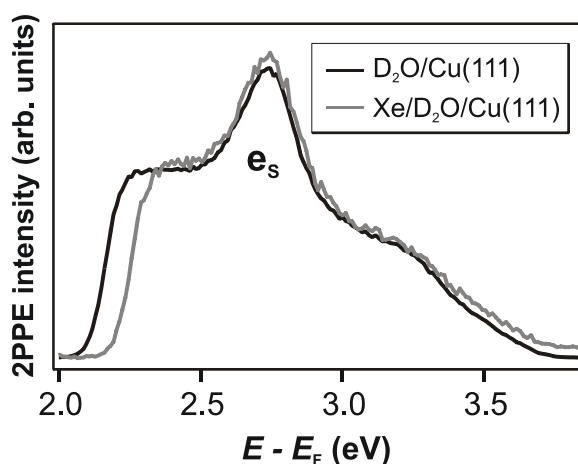

Fig. 4.16: *Xe Adsorption on top of the Ice Multilayer.* The peak position of e_S does not change upon Xe adsorption of 2 ML.

discussed. Fig. 4.17a illustrates the binding of solvated electrons *on top* of compact (left) and porous ice clusters (right). As shown in paragraph 4.1.2, peak shift *and* population decay are faster for the porous than for the compact clusters. It can be concluded that the higher density of D_2O molecules (i.e. the higher dipole density) leads to the slower back decay of the solvated electrons in the case of compact clusters. The more efficient screening of the ice dipoles underneath the electron (cf. Fig. 4.17a) results in longer lifetimes. This effect dominates over the influence of electron-metal distance, which can be higher for the porous clusters, as they are up to 1 BL higher than the compact islands.

The results of the empirical model calculation presented in 4.1.2, however, reveal the origin of the differing peak shifts and population transients. It was shown that the initial conditions for the solvated electrons in the porous and compact clusters, i.e. the initial decay time τ_0 and the influence of the solvent screening ΔE, are similar for both types of clusters. Furthermore, the energetic stabilization σ_S does not differ. The difference of the observables, peak shift and population decay, results *only* from the pre-exponential factor γ, which describes the *screening efficiency* with ongoing solvation. For compact ice, i.e. higher dipole density underneath the electron, γ is almost twice as large as for porous clusters (cf. Tab. 4.01). The larger number of water molecules that can contribute to the electron solvation leads to a faster screening and therefore to a slower back relaxation. The different energy-dependent transfer rates are also responsible for the different peak shift of porous and compact ice. Similar to the comparison of $D_2O/Ru(001)$ and $D_2O/Cu(111)$ (cf. 4.1.1), the considerably faster peak shift of the porous clusters Σ_S^P compared with Σ_S^C of the compact ice is due to the different energy dependence resulting from the different pre-exponential factor γ. The slower screening of the porous clusters results in a faster back decay of electrons at higher energies in the solvated electron distribution.
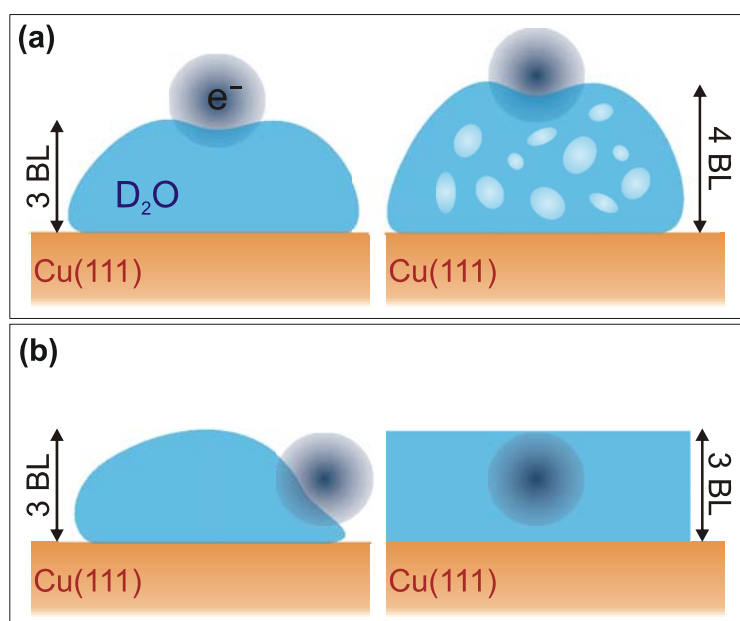

Fig. **4.17**: *Binding Sites of Solvated Electrons at the $D_2O/Cu(111)$ Interface.* a) Possible scenario for the solvated electron residing at the ice-vacuum interface. The higher dipole density in the case of compact clusters (left) leads to an enhanced screening of the excess electron compared with porous clusters (right). If the electrons bind on top of the clusters, this effect is stronger than the reduced wave function overlap with the metal due to the height difference of the clusters. b) The transition between cluster and layer growth – and therefore the surface-to-bulk transition – occurs at 2-3 BL coverage. As the compact clusters are 3 BL high, solvation at the cluster edges is probable.

Clusters and Multilayers: The observation of bulk-bound solvated electrons in the ice multilayer yields complementary information. The transition from ice clusters growth to adsorption in layers occurs at nominal coverages between 2 and 3 BL, [Gah03] and also the electron dynamics change in this coverage regime. [Gah02, Gah04] This changeover is, as shown above, mediated by the transition from the surface- to the bulk-bound solvated electron species. However, the actual *thickness* of the adsorbed ice does not differ: Electrons are surface-bound for 3-4 BL high clusters and bulk-bound starting from 3 BL thick amorphous ice films.

Comparison of the cluster data with the ice multilayer parameters (cf. Tab. 4.01) showed in 4.1.2, that the bulk-bound electrons in the ice layers are stabilized energetically with the same rate as the surface-bound electrons on the ice clusters. Besides that, the starting conditions of the solvated electrons are different: A stronger influence of the screening due to a higher ΔE and a larger initial decay time τ_0 show that the hydrated electron is better screened in the multilayer from the metal substrate right after photoinjection. In addition, the screening efficiency γ is also higher for the wetting multilayer. These observations disagree with the scenario in Fig. 4.17a, were the electrons bind *on top* of the ice clusters: The considerably higher number of water molecules *between* electron and substrate compared with the bulk-bound electron in the 3 BL thick film (Fig. 4.17b, right) should screen the excess electrons *more* efficiently, not less.

Another type of solvation site has to be taken into account: The Xe overlayer experiment clearly showed that the excess electrons bind at the ice-vacuum interface. However, this does not necessarily mean that the electrons solvate *on top* of the ice clusters as discussed on the basis of Fig. 4.17a. In fact, the electrons could also bind on the *edges* of the adsorbed ice clusters as sketched in the left panel of Fig. 4.17b. In this way, the transition from cluster to layer growth between 2 and 3 BL, which is governed by the surface-to-bulk transition of the solvation site, would not require a sudden appearance of a bulk-bound state in the 3 BL thick layers that is not apparent in the 3 BL thick clusters. As the coalescence of the clusters with increasing coverage finally leads to the layer formation, the transition to the bulk-bound state could occur without major changes in the electron-metal distance.

This scenario explains the enhanced screening of the excess electron in the ice layers compared with the clusters: The larger decay time τ_0, the relatively higher barrier $E_{barrier}$, and the larger screening efficiency γ in the case of the wetting layer suggest that the bulk-bound electron is considerably better screened from the metal due to a solvation shell, which completely surrounds it. Less water molecules contribute to the screening of the edge-bound electrons and thus the initial coupling to the metal is stronger and the screening efficiency lower. Hence, the edge-bound species as depicted in Fig. 4.17b appears to be the most probable scenario for electron solvation at the ice cluster-Cu(111) interface.

Facetted and Pyramidal Ice: It was shown in paragraph 4.1.2 that annealing of the ice cluster-covered Cu(111) surface to temperatures higher than 130 K leads to a dramatic structural transition of the clusters: The amorphous ice network reorients and forms well-ordered facetted islands. Further annealing finally leads to the development of pyramids on top of the facetted clusters. However, no significant changes of the photoelectron spectra were observed despite an intensity decrease of the e_S signal.

The STM is sensitive to structural variations in particular *on top* of the clusters. However, the structure of the cluster edges, which are almost perpendicular to the surface, i.e. almost parallel to the tip, are not well-resolved by STM studies. Thus, the scenario of edge-bound solvated electrons is further supported: If the solvated electrons resided on top of the clusters, significant changes of the photoelectron spectra would be expected due to the dramatic structural differences of compact, facetted, and pyramidal cluster surfaces. The structure of the cluster edges, in contrast, is not known. It is thus probable, that the coincidence of the electron dynamics for compact, facetted, and pyramidal clusters results from similar binding sites at the cluster edges. Furthermore, this scenario explains the intensity decrease of the solvated electron feature upon crystallization: As the ice islands coalesce increasingly upon crystallization (not shown, see [Meh05]), the number of cluster edges decreases. The analysis and comparison of the electron solvation dynamics at various $D_2O/Cu(111)$ interfaces including Xe overlayer experiments thus clearly shows that excess electrons solvate in the bulk of amorphous ice multilayers, but bind on the edges of supported ice clusters.

Impact on the Gas Phase Debate: As mentioned before, the surface vs. bulk solvation issue is controversially discussed for water anion clusters in the gas phase. Although the ice clusters investigated here are certainly perturbed by the presence of the metal template, the solvated electrons are certainly screened from the substrate to some extend. A comparison of the supported and the gas phase clusters is thus reasonable. As a value for the size of the gas phase clusters that can be compared with the supported ones, a sphere with the diameter of the cluster height is considered, i.e. $n \approx 30$. In this size regime, theory predicts surface-bound electrons only [Bar88, Tur05a], while the experimentalists propose the coexistence of surface- and bulk-solvated species for this cluster size. [Ver05a]

In the present work both, surface- and bulk-bound electrons, are observed for cluster/layer thicknesses which correspond to spherical $n \approx 30$ gas phase clusters. However, the shape of supported clusters deviates significantly from a sphere. In addition, an infinite laterally extending multilayer certainly cannot be set equal with a sphere. However, the outer solvation shells of the excess electron do not play a role for the initial localization right after photoinjection. The fact that electrons *can* find a favorable site for solvation and bind on the surface/in the bulk of the clusters/layers, which are 3 BL high, shows that electron hydration is *in principle* possible for both, the surface and the bulk site, of a $n \approx 30$ spherical cluster. In this sense, the presented results support the water cluster anion studies indicating a coexistence of surface- and bulk-bound species in this size range.

Having revealed the solvated electron's solvation site, the influence of the substrate, and the impact of ice morphology on its transfer and stabilization dynamics, the next paragraph focuses on the coupling strength of the hydrated electron to the metal states. The adequacy and applicability of the pictures of charge transfer introduced in section 2.1 will be discussed on the basis of time- *and* temperature-dependent 2PPE spectroscopy with the aim of determining the character of electron transfer from the transient hydrated electron state to a metal electrode.

4.1.4 Discussion: Tunneling vs. Marcus

Two different approaches to charge transfer at interfaces have been introduced in section 2.1, one taking into account the electron coordinate z (Landauer) and one considering primarily the solvent's degrees of freedom q (Marcus). It was shown that for a complete picture of charge transfer and solvation at interfaces, both coordinates have to be taken into account. However, depending on the degree of coupling between the excess charge and the metal states, one or the other picture is more applicable for the description of the pure transfer process: Either fluctuations of the solvent or solely the coupling matrix element rate-limit the electron transfer. A solvent rearrangement may occur due to thermal activation, but the direct coupling to substrate states is temperature-independent. The present paragraph discusses which coordinate, z or q, is relevant for the charge transfer process at amorphous ice-metal interfaces. To do so, determination of the temperature influence on the rate constant of the Marcus Theory is required. First, the temperature dependence of the classical Marcus Approach will be introduced, which is based on the assumption that the solvated electron is thermally equilibrated with its surrounding. Second, the model will be adjusted so as to describe the temperature dependence of a just photoinjected excess electron, followed by a discussion of charge transfer in the strong coupling limit. Finally, temperature-dependent measurements of the electron transfer dynamics at amorphous ice-metal interfaces will be presented and the rate-limiting step for charge transfer, solvent fluctuation or coupling strength, determined.

Truhlar's concept presented in paragraph 2.1.3 uses a two dimensional potential energy surface that reflects the system's evolution from a donor to an acceptor state as a function of solvent coordinate q and solute coordinate z, respectively. The corresponding 2D potential for electron transfer from the solvated state to a metal electrode has to take into account the spatial extend of the metal as well as the existence of a continuum of accepting states in the substrate on the other hand. Fig. 4.18a depicts a contour plot of the potential energy of the solvated electron (donor) state and the lowest unoccupied (acceptor) state of the metal as a function of lattice distortion q (vertical axis) and electron transfer coordinate z (bottom axis). The grey shaded area corresponds to the metal, the white background to the adsorbate layers. As for the proton transfer model in Fig. 2.06, horizontal cuts (blue dashed lines) result in the potential along the real space electron coordinate shown in panel (b). They describe the potential along z for a fixed solvent distortion. For increasing q (compare dark and light blue curves) the potential minimum decreases and the barrier maximum increases in energy. The increasing barrier reflects the higher degree of screening of the solvated electron with on-going solvation. Hence, these projections of the 2D potential illustrate the Landauer Model for ET: The charge
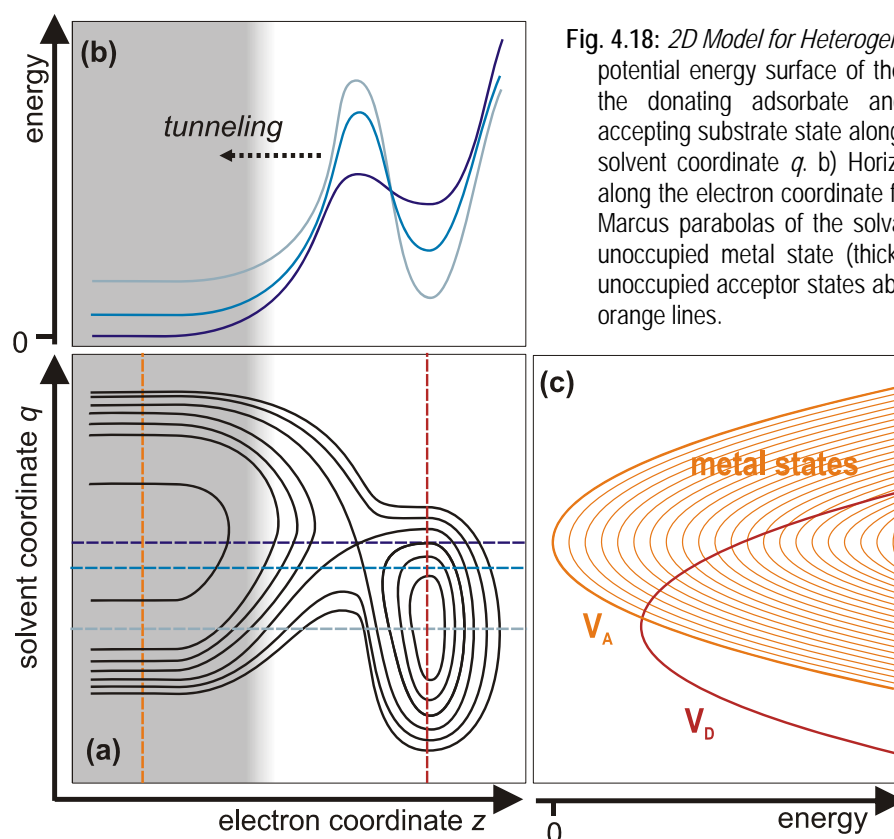
Fig. 4.18: *2D Model for Heterogeneous Charge Transfer.* a) 2D potential energy surface of the electron-solvent system for the donating adsorbate and the energetically lowest accepting substrate state along real space coordinate *z* and solvent coordinate *q*. b) Horizontal cuts give the potential along the electron coordinate for a fixed lattice distortion. c) Marcus parabolas of the solvated electron and the lowest unoccupied metal state (thick curves). The continuum of unoccupied acceptor states above V_A is denoted by the thin orange lines.

transfer along the electron coordinate and the increasing degree of solvation is taken into account by a transient tunneling barrier.

Projection of the 2D potential surface to the solvent coordinate *q* is depicted in Fig. 4.18c. Vertical cuts (orange and red dashed line in Fig. 4.18a) through the donor (solvated electron) and acceptor (metal) potential minima result in the Marcus Parabolas for donor (V_D) and acceptor (V_A), which were introduced in 2.1.2. These curves describe the course of potential energy of the electron *and* the potential energy stored in the lattice distortion as a function of solvent coordinate *q*. The potentials overlap in Fig. 4.18b, but do not in real space, as they are cuts through the 2D potential at different *z*. In addition to V_A (thick orange line) the metal offers a continuum of unoccupied states at higher energies which are sketched by thin, orange parabolas. At any intersection with V_D charge transfer to the metal may occur with a certain probability.

Taking into account this two-dimensional picture of heterogeneous charge transfer (HET), it becomes apparent that both coordinates influence the transfer rate of a solvated electron in ice layers on metal surfaces. Depending on the degree of solvation, the solvent coordinate *q* determines the real space potential along which the electron transfers (tunnels). The critical point of HET, however, is not *whether* tunneling occurs, but whether a solvent fluctuation *initiates* the tunneling. Such fluctuations are thermally activated and occur more frequently for higher temperatures. Due to thermal activation, the system fluctuates to a lower *q*, at which charge transfer occurs along *z*. This process is termed thermally activated tunneling. [Rog85]

As the thermally activated fluctuations lead to a change of solvent coordinate q, it is appropriate to discuss the temperature dependence of the transfer rate on the basis of Marcus Theory. As introduced in paragraph 2.1.2, the charge transfer probability from a molecular donor to the metal acceptor follows: [Mil95]

$$k_{hetero} = \int_{-\infty}^{\infty} \frac{2\pi}{\hbar} \cdot \left\langle V_{DA}(E) \right\rangle^2 \cdot \left(1 - f(E)\right) \cdot \rho(E) \cdot \left(\frac{1}{4\pi\lambda k_B T} \right)^{\frac{1}{2}} \cdot \exp\left(-\frac{\left(E + \left(\lambda + \Delta G^0\right)\right)^2}{4\lambda k_B T} \right) dE \ . \quad (4.6)$$

Note that this description is based on the assumption that the system is fully equilibrated, i.e. Boltzmann-distributed around the minimum of the donor potential V_D. As the integrand includes a Gaussian around $\lambda + \Delta G^0$, the most simple case to discuss occurs when the density of states $\rho(E)$ and the coupling matrix elements $V_{DA}(E)$ are constant. Fig. 4.19 depicts the two resulting scenarios: (a) Equation (4.6) becomes independent of temperature if $(\lambda + \Delta G^0) < 0$ and if the Gaussian is narrow enough so that it is not considerably cut by the Fermi Function (1-$f(E)$), i.e. $\left(\lambda + \Delta G^0\right) + \sqrt{\lambda k_B T} << 0$.[80] In other words, the temperature dependence cancels out, because the donor potential is cut by acceptor parabolas at all energies down to its minimum. Thermal activation is not required for ET. (b) If, instead, $(\lambda + \Delta G^0) > 0$, the Fermi Function cuts
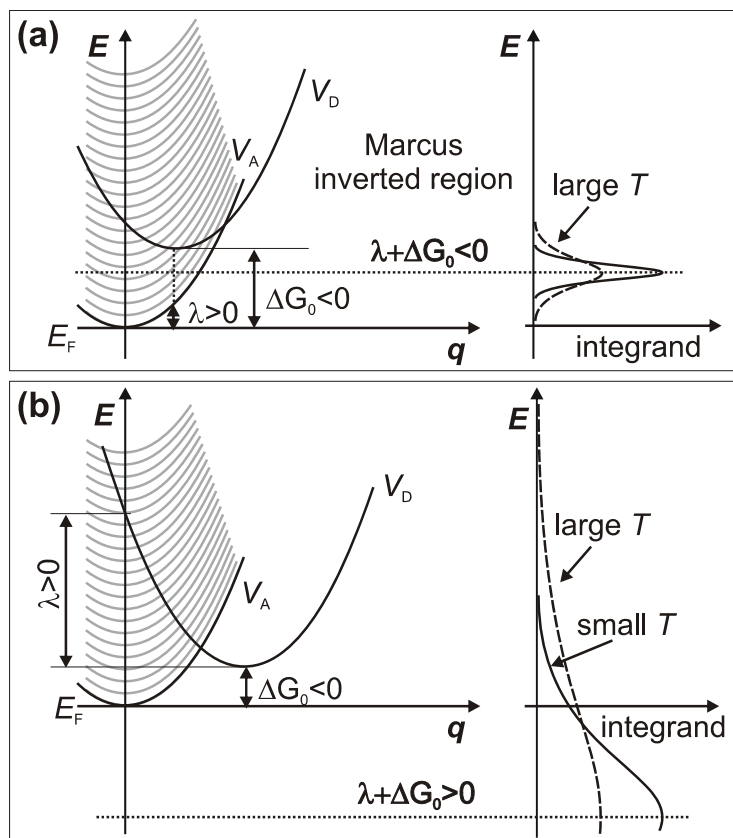

Fig. 4.19: *Influence of Temperature on HET from an Equilibrated Donor.* a) In the Marcus inverted region (($\lambda + \Delta G^0$)<0) the HET is independent of temperature as the donor parabola is intersected by acceptor parabolas at any energy. Constant V_{DA} and $\rho(E)$ are assumed. b) If ($\lambda + \Delta G^0$)>0, i.e. the donor potential minimum lies underneath the lowest metal parabola, charge transfer from the equilibrated donor to the metal is temperature dependent.

---

[80] The infinite integral of a Gaussian is proportional to its width. As the Gaussion is $\sqrt{4\lambda k_B T}$ wide in (4.6), the temperature dependence cancels out due to the prefactor.

the Gaussian significantly and the transfer rate increases with temperature as illustrated in Fig. 4.19b. Demonstratively spoken, transfer of the equilibrated electron population around the donor potential minimum *requires* thermally activated solvent fluctuations to reach the intersection with the lowest-lying acceptor parabola.

The temperature dependence of equation (4.6) appears to depends on the relative position of the V_D and V_A minima, i.e. whether the system is in the Marcus inverted region or not. However, (4.6) is derived for thermally equilibrated, Boltzmann-distributed systems. In other words, the electron has

Fig. 4.20: *Thermally Activated Electron Transfer.* The nuclear barrier of the equilibrium description is reduced by $E_S + \Delta G^0$.

equilibrated in the donor potential (i.e. in the solvation shell) and the probability to find it at any q follows Boltzmann Statistics. In the case of the just photoinjected, hot excess electron at the ice-metal interfaces investigated here, this is not necessarily the case. The system *proceeds* along q on its way to the potential minimum. The constant nuclear barrier ΔE^* derived in paragraph 2.1.2 becomes dependent on the binding energy of the solvated electrons E_S in their respective (quasi-equilibrated) state of solvation. The transfer constant thus becomes a function of the energy of the solvated electron E_S:

$$k\left(E_S\right) \propto \int \langle V_{DA}\rangle^2 \cdot \left(1 - f\left(E\right)\right) \cdot \rho\left(E\right) \cdot \left(\frac{1}{T}\right)^{\frac{1}{2}} \cdot \exp\left(-\frac{\Delta E_{hot}^*\left(E, E_S\right)}{k_B T}\right) dE \tag{4.7}$$

As illustrated in Fig. 4.20, ΔE_{hot}^* describes the nuclear barrier that has to be overcome when an electron with the distinct energy $E_S(q)$ on the donor potential (at $q<q_0$) transfers to an acceptor state at the energy E. The nuclear barrier of the fully equilibrated system, derived in 2.1.2,

$$\Delta E_{equi}^*\left(E\right) = \frac{\left(E + \left(\lambda + \Delta G^0\right)\right)^2}{4\lambda} \tag{4.8}$$

is reduced by the energy difference of the solvated electron to the donor parabola minimum $(E_S + \Delta G^0)$

$$\Delta E_{hot}^*\left(E, E_S\right) = \Delta E_{equi}^*\left(E\right) - \left(E_S + \Delta G^0\right) \tag{4.9}$$

This reduction of the barrier compared with the equilibrium description leads to an additional exponential factor in the transfer rate integral compared with equation (4.6):
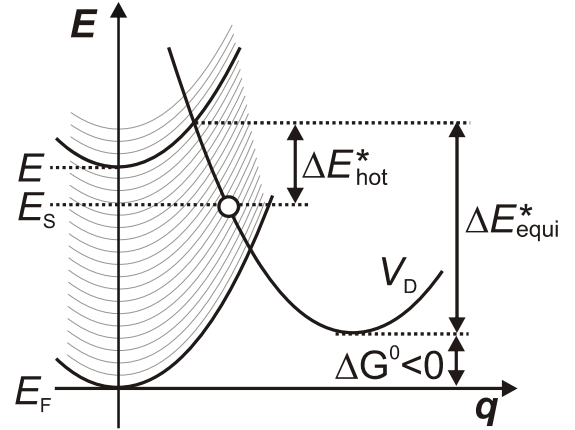
$$k(E_S) \propto \int \langle V_{DA} \rangle^2 \cdot (1 - f(E)) \cdot \rho(E) \cdot \left(\frac{1}{T}\right)^{\frac{1}{2}} \cdot \exp\left(\frac{E_S + \Delta G^0}{k_B T}\right) \cdot \exp\left(-\frac{\left(E + \left(\lambda + \Delta G^0\right)\right)^2}{4\lambda k_B T}\right) dE \quad (4.10)$$

The term $E_S + \Delta G^0$ is always positive and becomes zero when the solvated electron is fully equilibrated. It introduces a temperature dependence of the transfer rate, which is *not* cancelled out as was the case for the equilibrium description in the Marcus inverted region (Fig. 4.19a). In conclusion, in this picture, where constant V_{DA} and $\rho(E)$ are assumed, charge transfer is *always* temperature-dependent as long as the system has not reached the V_D minimum, i.e. $E_S + \Delta G^0 = 0$.

As mentioned above, the above discussion is based on the assumption that both, V_{DA} and $\rho(E)$, are constant in energy. However, for a solvated electron that subsequently changes its degree of confinement, a constant coupling matrix element V_{DA} certainly does not hold true. The coupling instead decreases significantly upon solvation, as already shown in paragraph 4.1.1. Thus, the variation of $V_{DA}(E)$ in equation (4.6) also causes a temperature dependence of the fully equilibrated system, even when the system is in the Marcus inverted region and in thermal equilibrium.

The above discussion of the impact of temperature on the transfer rate, including all derived formulas, is based on the assumption that the ET reaction occurs in the *weak coupling limit*. As discussed in paragraph 2.1.2, the coupling matrix element V_{DA} is considered to be very small: The avoided crossing of donor and acceptor potential is negligible. For strong electronic coupling, however, splitting and repulsion result in a new potential that connects donor and acceptor, so that ET can occur adiabatically (cf. Fig. 2.04). [Mil95] Fig. 4.21 sketches the Marcus Potentials for the heterogeneous charge transfer problem with strongly varying coupling matrix elements at a molecule-metal interface. The inset enlarges the crossing point regions of interest. In the strong coupling limit the splitting due to avoided crossing leads to the formation of new potentials connecting donor and acceptor states (red curves). As the coupling is reduced upon solvation due to the stronger screening of the electron, the splitting is subsequently reduced and a nuclear barrier evolves between donor and acceptor (violet curves). The weak coupling limit is reached when the splitting becomes negligible (blue curve). Transfer to lower-lying metal curves can be treated non-adiabatically as
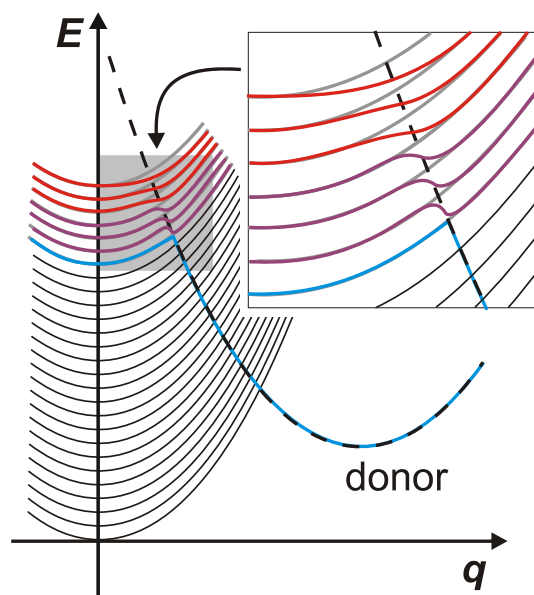

Fig. 4.21: *Strong and Weak Coupling.* For a just photoexcited excess electron in front of a metal surface, the coupling to metal states changes subsequently with ongoing solvation. The transition between the strong and the weak coupling limit is governed by a reduction of potential splitting due to avoided crossing.

discussed in the beginning of this paragraph. As no nuclear barrier is apparent for the *strong coupling limit*, charge transfer is not thermally activated (red curves). Solvent rearrangement is not the rate-limiting step anymore. The transfer is solely determined by the coupling matrix element V_{DA} and mediated by tunneling through the wave function overlap with metal states. The interfacial electron transfer is temperature-independent.

In this sense, the degree of temperature dependence offers information about the coupling of the solvated electron to the metal states. To determine in which regime of electronic coupling, strong or weak, the electron transfer occurs at ice-metal interfaces, temperature-dependent 2PPE measurement were performed for the $D_2O/Cu(111)$ and $Ru(001)$ systems. Fig. 4.22 depicts the population dynamics of solvated electrons in D_2O layers on the $Cu(111)$ and the $Ru(001)$ surface at different temperatures. For both data sets no temperature dependence of the electron back decay to the metals is observed within the first half picosecond.[81] Based on the above discussion it can be concluded that the electron transfer at the investigated ice-metal interfaces is *not* thermally activated. This result shows that the HET observed here occurs in the *strong coupling limit*. The solvated electrons are, despite their localized

Fig. 4.22: *Temperature Dependence of ET for D₂O/Cu(111) and Ru(001).*
Population dynamics of solvated electrons at amorphous ice-metal interfaces. The decay is independent of temperature between 25 and 119 K. Inset: Shift of the e_S maximum as a function of time delay for D₂O/Cu(111). No temperature dependence is observed.
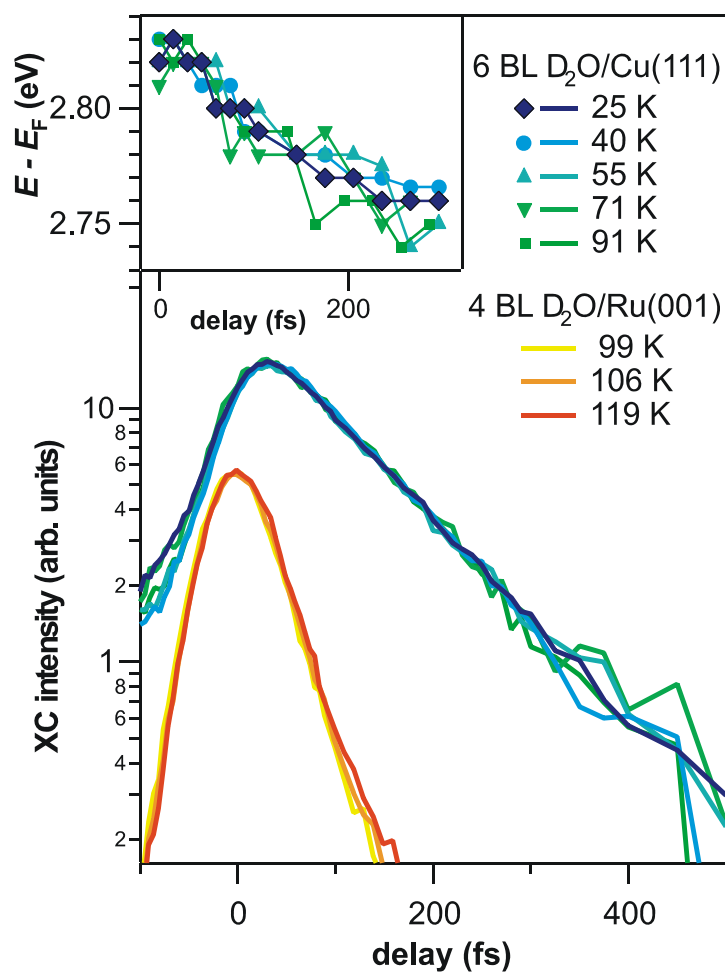
character, still strongly coupled to the metal states. Direct charge transfer to the metal states is considerably more favorable than thermally activated tunneling at smaller q. Furthermore, the absence of a temperature dependence in the time window of 500 fs for $D_2O/Cu(111)$ shows that the *change* of coupling matrix element is not large enough to achieve a cross-over to the weak coupling limit, were charge transfer is thermally activated.[82] The inset of Fig. 4.22 depicts the peak shift of the solvated electron distribution as a function of pump-probe time-delay. Obviously, the electron stabilization, i.e. the progression along q, is also temperature-independent. Thermally activated molecular reorientations are thus not required to initiate the binding energy gain of ~200 meV/ps.

Conclusions

In the present section electron transfer and solvation dynamics at amorphous ice-metal interfaces were discussed. To achieve a complete picture of the underlying fundamental processes, the electron dynamics were systematically studied with respect to the substrate influence, impact of ice structure, solvation site, and temperature. It was shown, that charge transfer occurs at the investigated interfaces in the strong coupling limit, i.e. that charge transfer does not require nuclear rearrangement due to thermal activation. However, a transition between the substrate-dominated and the barrier-determined regime of ET was observed and discussed in paragraph 4.1.1. In the former case, the back transfer of the solvated electrons to the metal was determined by the substrate's electronic properties (bandgap, DOS). Subsequently, a transient barrier forms at the ice-metal interfaces, which reduces the wave function overlap of the hydrated electron with the metal states. The tunneling probability with this barrier becomes the rate-limiting step for electron back decay.

Furthermore, with the aid of sophisticated STM experiments done by K. Morgenstern and M. Mehlhorn, five different structures of ice clusters on the Cu(111) surface were identified, porous and compact amorphous, facetted, pyramidal, and crystalline ice. The impact of the structural transitions on the electron solvation dynamics in combination with Xe overlayer experiments revealed that the hydrated electrons preferentially bind on the *edges* of the adsorbed ice clusters. In this manner a surface-to-bulk transition of electron solvation could be observed, as excess electrons solvate in the bulk of closed ice multilayers.

In conclusion, a consistent picture for electron transfer and solvation at amorphous ice-metal interfaces has been developed. As mentioned before in section 2.3, the transition to crystalline ice layers on metal surfaces is governed by significant changes in the interfacial electron dynamics. While the strongly coupled electrons in the amorphous ice adlayers decay to

---

[81] As the temperature had to be kept constant during the measurement, it was not possible to acquire enough statistics to achieve information about later delays (3.2.1)

[82] This is different for the NH₃/Cu(111) system discussed in chapter 5, where the transition between the weak and strong coupling limit it is observed in real time.

the metal on femtosecond timescales before solvation is completed, trapped electrons survive in the crystalline ice layers for several minutes. In addition to their extraordinarily long lifetime, their stabilization continues on this macroscopic timescale and exhibits a significant dependence on temperature. In other words, the transition from amorphous to crystalline is accompanied by the transition from the strong to the weak electronic coupling limit.

4.2 Freezing Hot Electrons in Crystalline Ice

The electron solvation dynamics at ice-metal interfaces change significantly upon the transition from amorphous to crystalline ice layers. Instead of lifetimes on the order of 100 fs (see previous section) the electrons are much more efficiently screened from the metal substrate and survive in the crystalline adlayer for several minutes. However, the *formation* dynamics of these ultralong-living solvated electrons have not been observed yet. Paragraph 4.2.1 will show that the electron dynamics *are* observable on the femtosecond timescale and evolve until the late time regime (minutes) is reached. The present work therefore reveals electron solvation dynamics ranging over 17 orders of magnitude in time. It will be discussed in 4.2.2 that the description of this ultralong evolution of electron solvation requires the introduction of a so-called "stretched exponential" approach, which allows for the description of dynamics over all timescales observed. In addition to the significant temporal evolution, the trapped, ultralong-living electrons exhibit a notable temperature dependence. It will be shown that progression along the solvent coordinate q proceeds thermally activated by flipping of water molecules. Moreover, it will be shown that the time constant for electron solvation is temperature-dependent and can be associated with a friction coefficient of a highly damped harmonic oscillator.

4.2.1 Electron Solvation from Femtoseconds to Minutes

Crystallization of $D_2O/Ru(001)$ leads to the formation of an ultralong-living electronic interfacial state, which is characterized by trapped, efficiently screened electrons at the ice-vacuum interface. [Gah04] The dynamics on minute timescales of this state e_T were introduced in paragraph 2.3.2 and investigated in detail in C. Gahl's dissertation. The *formation dynamics* of the trapped electrons, however, have not been studied thus far. Only photon energy dependent measurements of the excitation probability indicate that charge injection occurs via the $n = 1$ image potential state of the $D_2O/Ru(001)$ interface. [Gah04, Bov07] In the present work the electron trapping is directly observed in real time, i.e. on fs-timescales. As the bad signal-to-background ratio (~1%) of the trapped electron dynamics requires a sophisticated data analysis, this paragraph will first introduce the concept of a photostationary state before turning to the description of background subtraction. Finally, the ultrafast formation dynamics will be presented, showing that electron solvation proceeds at crystalline ice-metal interfaces across 17 orders of magnitude in time.

Photostationary State: The main difficulty for the observation of the ultrafast dynamics of the ultralong-living trapped electrons in crystalline ice is the very low intensity of this species. Fig. 4.23 (top) presents 2PPE spectra of a crystalline multilayer $D_2O/Ru(001)$. In contrast to the spectra shown before, only UV light was employed to measure these data, i.e. the pump and the probe photon have the same energy. The spectra exhibit four features: Hot electrons at the secondary edge, the d-band, the $n = 1$ image potential state, and the peak of the ultralong-living trapped electrons e_T (see 2.3.2). The spectra were taken for different laser pulse durations between 100 and 280 fs. The bottom panel of Fig. 4.23 presents the respective peak intensities: As expected for a two-photon process (pump and probe within the same pulse) the intensity of d-band and IPS decreases linearly with the inverse square of the pulse duration, i.e. with the temporal photon density. However, the peak e_T is not affected by the pulse elongation: Its intensity remains constant. It can be concluded that excitation and probing are not correlated, i.e. they occur during different laser pulses. This observation suggests that the excitation and probing probability are very low, because a dependence on the temporal photon density would be visible otherwise. Despite the small excitation

Fig. **4.23**: *2PPE Spectra of Crystalline $D_2O/Ru(001)$.* Top: UV-only spectra for different pulse durations. The intensity of hot electrons, d-band, and IPS changes upon pulse elongation. The feature e_T does not vary. Bottom: Relative peak intensities as a function of inverse square of the pulse duration. IPS and d-band are excited and probed within the same pulse, e_T in different pulses (modified from [Gah04]).

efficiency, the 2PPE intensity of the e_T feature is, in Fig. 4.23, considerably higher than for the IPS and the d-bands. The large signal is reached only due to the long lifetime of the trapped electrons: Every subsequent UV laser pulse excites electrons to the long-living state e_T, each having a low decay probability. The *accumulation* of electron population leads to the macroscopic signal of trapped electrons. The interplay of excitation and probing probability results in the formation of a photostationary state as discussed in the following.

The long residence time of the trapped electrons allows the description of the population dynamics assuming quasi-continuous wave irradiation of the sample. The change of population n of the e_T state then follows the differential equation

$$\frac{\partial n}{\partial t} = -\frac{1}{\tau} \cdot n + a \cdot I \cdot (N - n) - b \cdot I \cdot n \qquad (4.11)$$
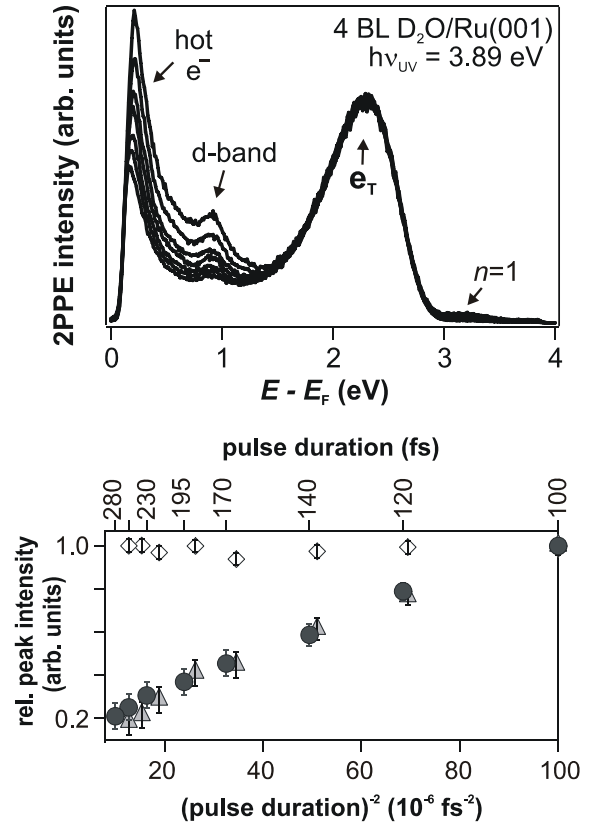
where τ denotes the electron lifetime, N the total number of solvation sites, $a \cdot I$ the laser intensity-dependent excitation probability and $b \cdot I$ the probing probability. The population increases according to:

$$n(t) = \frac{\alpha N}{\frac{1}{\tau} + \alpha + \beta} \cdot \left(1 - \exp\left[-\left(\frac{1}{\tau} + \alpha + \beta \right) \cdot t \right] \right) \text{ with } \alpha = a \cdot I \text{ and } \beta = b \cdot I \qquad (4.12)$$

As shown in [Gah04] $1/\tau$ can be neglected for the low laser intensities (<1 mW) used so that excitation and probe probability determine the rise time of the e_T intensity. In accordance with this description, a linear dependence of $(\alpha + \beta)$ on the employed laser fluence was observed. Under the employed experimental conditions the rise time is on the order of 0.1 s. [Gah04]

The formation of the photostaionary state as described above enabled the time-resolved experiment on macroscopic timescales shown in Fig. 2.11. The pump-probe scheme of this measurement is depicted in the top panel of Fig. 4.24: A sequence of UV laser pulses irradiated the sample for 10 s to ensure equilibrium between pumping and probing by UV photons. The sample was left in the dark for the desired time delay (e.g. 60 s as shown in Fig. 4.24, top) and subsequently probed with visible light. The stabilization dynamics of e_T, which occur during this delay, are illustrated by the dotted line in Fig. 4.24 (top panel). In this manner, the 2PPE spectra in Fig. 2.11 for time delays between 1s and 630 s were achieved. The spectrum at 0.1 s results from the rate equation approach described above: After irradiation of the sample with UV light only, until the 2PPE intensity reaches its photostationary state, the *average* age of the probed electrons is, according to equation (4.12), the time constant for the exponential rise of the e_T population of 0.1 s and is described by

$$\tau_a = \frac{1}{\alpha + \beta} \qquad \text{for} \qquad \tau \gg 1 \qquad (4.13)$$

Background Subtraction in the Ultrafast Experiment: The implementation of pump-probe experiments of an ultralong-living electronic state is complicated by three factors: (i) Low excitation probability, (ii) a strong, constant background due to the trapped electrons, and (iii) a *time-dependent* background around zero time delay due to electronic states decaying on fs-timescales. These difficulties have prohibited the study of the trapped electron formation dynamics in the past. Better statistics and adjusted data analysis, however, makes the observation of electron injection on ultrafast timescales in the present work possible. To achieve these results, the difficulties (i)-(iii) had to be identified and dealt with as discussed in the following.
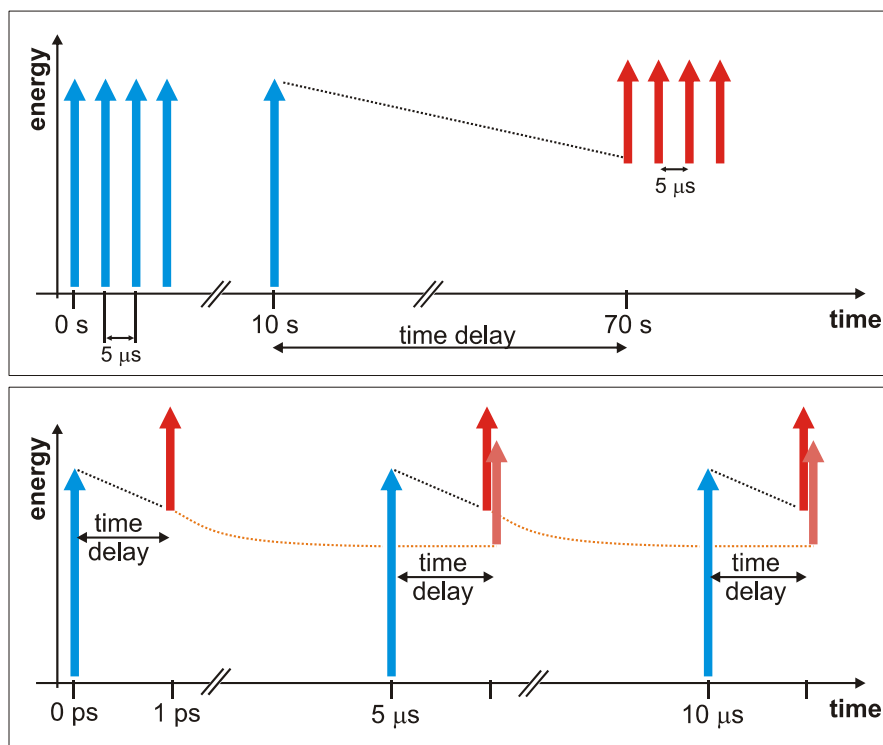
Fig. 4.24: *Pump-Probe Schemes for Ultrafast and Ultraslow Dynamics.* Top: For 2PPE on macroscopic timescales the sample is irradiated for 10 s, left in the dark for the desired time delay, and the electron population is finally probed by VIS light. Bottom: The ultrafast dynamics are monitored by one VIS pulse that follows the single exciting UV pulse. The signal is overlapped by electrons that have been excited 5 μs previously. See text for details.

(i) Low Excitation Probability: In contrast to the pump-probe experiment on macroscopic timescales, where a sequence of UV pulses excite a large number of trapped electrons (Fig. 4.24, top), the intensity in the ultrafast experiment is limited by the excitation density of only *one* UV laser pulse, which is, as discussed further above, very low. As depicted in the bottom panel of Fig. 4.24, the excited electron population is probed by VIS photons after the desired time delay in the femto- and/or picosecond time domain. This experiment is repeated every 5 μs due to the repetition rate of the laser. As the low excitation probability of e_T is an intrinsic problem, the experiment was performed with very good statistics[83] to improve the signal-to-noise ratio.

---

[83] The data was aquired five times longer than in an ordinary ultrafast pump-probe experiment (see, for example, Fig. 4.01).

(ii) <u>Constant Background</u>: As the probing probability of the visible light $\gamma = c \cdot I$ is – as β for the UV light – certainly smaller than unity, the excited electron population by the first UV pulse at $t = 0$ is not completely probed by the subsequent VIS pulse after the desired time delay (1 ps in Fig. 4.24). The residence time of the remaining trapped electrons is larger than the inverse laser repetition rate of 5 μs. Thus, these electrons are further stabilized until the next UV pulse reaches the sample, as illustrated by the dotted orange curve. When the second VIS pulse reaches the sample, it probes not only the "freshly" excited electrons, but also – with the probability γ –the "old" ones. This signal overlaps with the fs-dynamics of the just injected electrons. This background signal, however, does not exhibit dynamics on fs-timescales[84] so that the constant background can be subtracted from the data. Nevertheless, this constant signal is very large compared with the time-dependent signal of e_T as depicted in Fig. 4.25. It is apparent from the inset, which depicts the 2PPE intensity on a logarithmic scale, that the signal of interest amounts to only ~1 % of the total intensity.
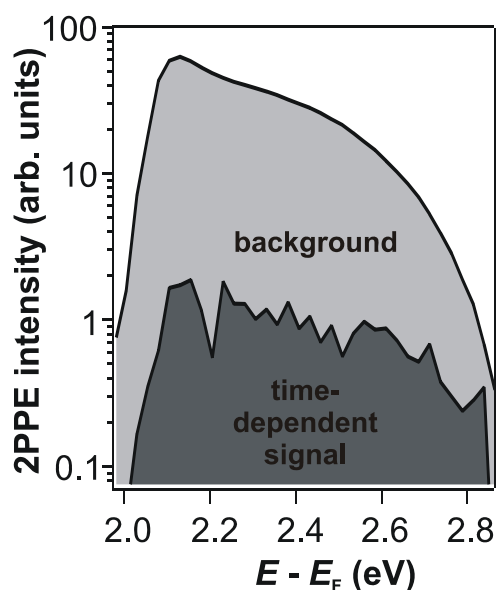

Fig. 4.25: *Illustration of Signal-to-Background Ratio.* The time-dependent signal of the trapped electrons amounts to only ~1% of the constant background.

It is remarkable that despite this enormous background, trapped electrons could be identified: Fig. 4.26 depicts time-dependent 2PPE spectra of crystalline $D_2O/Ru(001)$. The temporally constant background (cf. Fig. 4.25) has already been subtracted from the data. However, at early delays ($t < 500$ fs), the spectra in Fig. 4.26 are dominated by the time-dependent background of hot electrons at the secondary edge, the d-bands, and the first two image potential states of the $D_2O/Ru(001)$ interface. As these signals vary with increasing time delay, a subtraction of this time-dependent background is more difficult (see further below). Nevertheless, at 0.5 ps all intensity from this correlated background signal has vanished, and the remaining 2PPE intensity close to the secondary edge can be assigned to the ultralong-living trapped electrons e_T. As mentioned before in paragraph 2.3.2, a photon energy dependence of the e_T excitation suggested that these excess electrons are injected into the ice layer via the $n = 1$ image potential state. [Gah04] As the state lies at 3.15 eV and the trapped electrons are observed at $E - E_F = 2.3$ eV, the photoinjected electrons must in crease their binding energy by almost 1 eV within the first half picosecond after excitation.

---

[84] It is assumed that electrons probed after 5 μs are comparably stabilized as – for example – electrons probed after 5.000001 μs or 4.999999 μs.

(iii) <u>Time-Dependent Background</u>: As mentioned above, knowledge of the *formation* dynamics of the ultralong-living state is desirable, as the injection process has only been determined indirectly thus far. The *correlated* background signal of d-band, $n = 1$ IPS, and hot electrons varies as a function of time delay between the laser pulses. Thus, background subtraction is not easy. The essential point is to note that none of these features exhibits *dynamics* at positive delays: Hot electrons and d-band are excited by VIS light and probed by UV photons; the $n = 1$ has a vanishing lifetime smaller than 5 fs.[85] Hence, their intensity decreases to positive delays (UV pumps, VIS probes) similar to the cross-correlation function of the two laser pulses. *Any* other dynamics occurring to positive delays must be due to the formation dynamics of the trapped electrons. The background subtraction is thus performed taking into account that the intensity decrease of the autocorrelation function follows a sech^2.
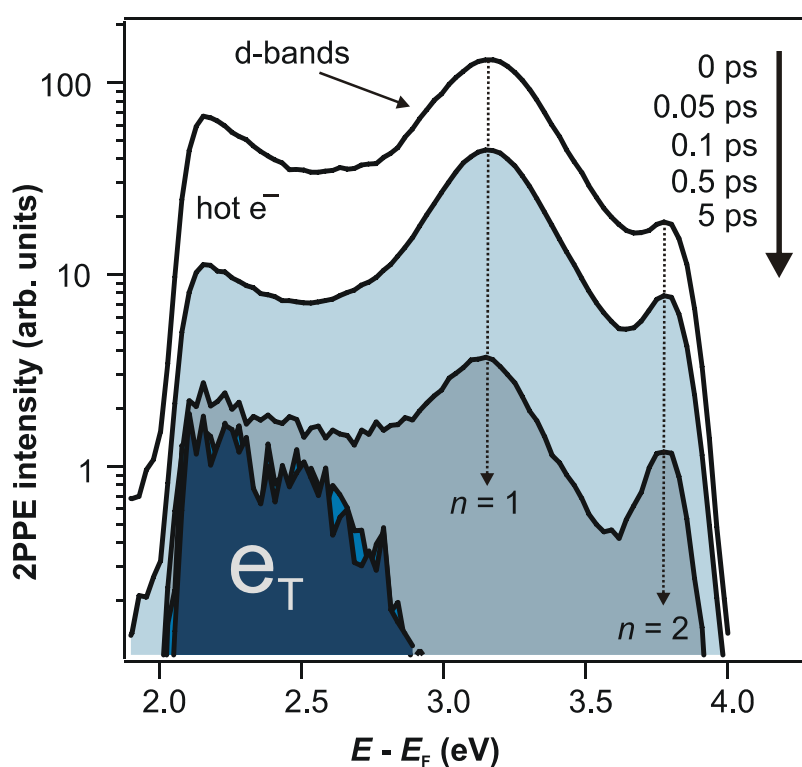

Fig. **4.26**: *Electron Dynamics in Crystalline D$_2$O on Femtosecond Timescales.* At early delays the signal of the ultralong-living electrons is overlapped by the high intensity of IPS, d-band and hot electrons. After 0.5 ps the time-dependent background has decayed and e$_T$ is clearly discerned.

---

[85] The $n = 2$ indeed exhibits a finite lifetime at positive delays, but lies at considerably higher energies (> 3.5 eV). Thus, these dynamics do not interfer with the e$_T$ dynamics.

Formation Dynamics: Fig. 4.27 presents the population dynamics after time-dependent background subtraction. The data describes all dynamics which deviate from the autocorrelation function shape, i.e. all dynamics that result from trapped electrons in the ice. The $n = 1$ IPS intensity was obtained by integrating between $E - E_F = 2.9$ eV and 3.5 eV (circles). The spectral feature looses more intensity than it should due to the bare autocorrelation function. This additional intensity loss occurs within ~50 fs.[86] The intensity of e_T (diamonds, integrated between 2.0 eV and 2.9 eV), in contrast, increases within ~20 fs and then subsequently decreases. The correlation of the IPS intensity decrease and the e_T increase clearly demonstrates the population of the ultralong-living state at 2.3(2) eV via the image potential state at 3.15 eV. Previously, this process of electron injection was derived only implicitly on the basis of an excitation photon energy dependence. [Gah04] With the present analysis, the *direct observation* of this formation process of the ultralong-living electrons is possible.
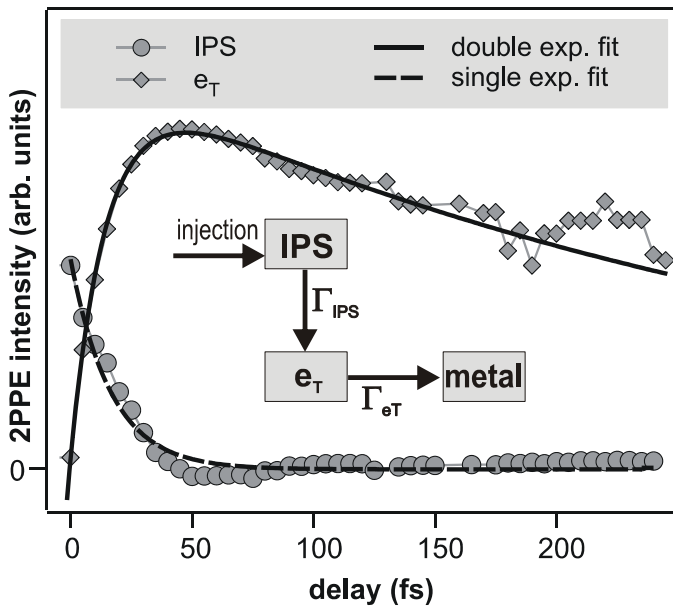

Fig. 4.27: *Population Dynamics of Ultralong-Living Electrons.* The population of the trapped electron state (diamonds) e_T increases as the population of the IPS (circles) decreases. Solid and dashed lines are least square fits to e_T and IPS, respectively. See text for details.

The sketch in Fig. 4.27 illustrates the underlying mechanisms: Electrons are injected into the ice layer via the IPS at $t = 0$. With a certain probability Γ_{IPS} the electrons localize at pre-existing favorable sites in the crystalline ice adlayer and decay with the rate Γ_{eT} back to the metal substrate. Accordingly, the populations of IPS and e_T follow the rate equations:

$$\dot{n}_{IPS} = -\Gamma_{IPS} \cdot n_{IPS} \qquad \text{and} \qquad \dot{n}_{eT} = -\Gamma_{eT} \cdot n_{eT} + \Gamma_{IPS} \cdot n_{IPS}, \qquad (4.14)$$

which leads to the population transients

$$n_{IPS}(t) = A_{IPS} \cdot \exp[-\Gamma_{IPS} \cdot t] \quad \text{and} \quad n_{eT}(t) = A_{eT} \cdot (\exp[-\Gamma_{IPS} \cdot t] - \exp[-\Gamma_{eT} \cdot t]). \qquad (4.15)$$

---

[86] This is possible despite the short lifetime of the IPS (< 5 fs): Due to the finite pulse duration, the IPS intensity amounts to 27 % after 50 fs and to 1 % after 100 fs, of the maximum amplitude. This decay due to localization to e_T is not seen in an ordinary XC trace of the IPS as it adds up to only a few percent of the absolute IPS intensity.

The least square fits of these functions to the IPS and e_T transients are represented by the solid and dashed lines in Fig. 4.27, respectively. According to the fits, the population exchange between IPS and e_T occurs with a time constant of $\Gamma_{IPS}^{-1} = 16(5)$ fs and the initial decay time of trapped electrons back to the Ru(001) substrate is $\Gamma_{eT}^{-1} = 320(10)$ fs.[87] The above experiment thus shows the initial formation dynamics of the ultralong-living electrons in crystalline ice on Ru(001). Moreover, the observation of e_T at 2.3(2) eV after 50 fs demonstrates that the electrons must be trapped in *pre-existing* traps in the ice adlayer after injection via the IPS at 3.15 eV. Dynamic polaron formation, requiring solvent reorganization to form the potential minimum, is a frequently discussed alternative process of electron localization. [Ge00, Szy05] However, this mechanism of charge localization can be excluded, as molecular rearrangement leading to a binding energy gain of almost 1 eV is not possible within such a short time range, because it requires considerable nuclear motions.

The previous measurement enables the combination of the long-time peak shift of the trapped electrons, which was shown in Fig. 2.11, with the data obtained above. The entire observed shift of the peak maximum, starting at 50 fs and continuing up to 10 min, is depicted in Fig. 4.28. Note that the data is plotted versus a *logarithmic* time axis.[88] Remarkably, the combination of the ultrafast 2PPE experiment with the pump-probe measurement on minute timescales allowed for the observation of electron solvation dynamics over a range of *17 timescales*:[89] Charge injection occurs on fs-timescales and energetic stabilization continues for 10 min.

The electron dynamics in crystalline ice adlayers thus include all timescales of interest: In the ultrashort time domain electrons decay by resonant tunneling to the metal (cf. Fig. 4.27). The solvation of the remaining trapped electrons continues, due to rearrangement of water molecules, from femtoseconds to minutes. Such energetic has been observed before for amorphous ice layer in the fs to ps time regime (cf. section 4.1). However, in comparison, the dynamics observed at the crystalline ice-metal interface are 14 orders of magnitude slower. Hot electrons in the metal, which are transferred to the ice via the IPS are obviously very efficiently screened from the substrate in preexisting traps even in the early stages of solvation. The significant decoupling from the metal makes the extraordinary long lifetimes and thus the continuous solvation ("*freezing*") possible.

---

[87] At later delays ($t > 400$ fs) the decay slows down significantly due to enhanced screening of the electrons in the ice layer (not shown).

[88] Vertical error bars result from the width of the e_T peak. In the case of the blue and green data points they are larger at lower energies, as the peak is cut by the secondary edge.

[89] The green data point at 5 μs results from the constant background of e_T (see Fig. 4.25). Its main contribution is considered to be 5 μs "old": It results from trapped electrons excited by the preceding UV pulse. Determination of the second green data point benefits from the formation of a photostationary state: Such equilibrium is also reached when irradiating the sample with UV and VIS light. In contrast to the UV-only experiment discussed above, the probing probability of the visible light γ has to be introduced into the equations (4.11) and (4.12). As the VIS photons only depopulate e_T, but do not inject electrons, the average "age" of the trapped electrons (4.13) in the photostationary state is reduced to $\tau_a = (\alpha+\beta+\gamma)^{-1} = 5$ ms. (Comparison of the e_T intensity UV+UV spectra with UV+VIS spectra, where e_T occurs twice (probed by UV and VIS), enables determination of α, β, and γ.)

Fig. 4.28: *Dynamics Ranging Over 17 Orders of Magnitude in Time.* Peak shift of the spectral feature of the trapped electrons e_T as a function of time, ranging from 10^{-14} s to 10^2 s. Red markers originate from the pump-probe experiment on minute timescales, blue and green diamonds from the ultrafast measurement. (See [89] for details) Black curve results from a model calculation considering stretched-exponential behavior, which will be introduced in 4.2.2.
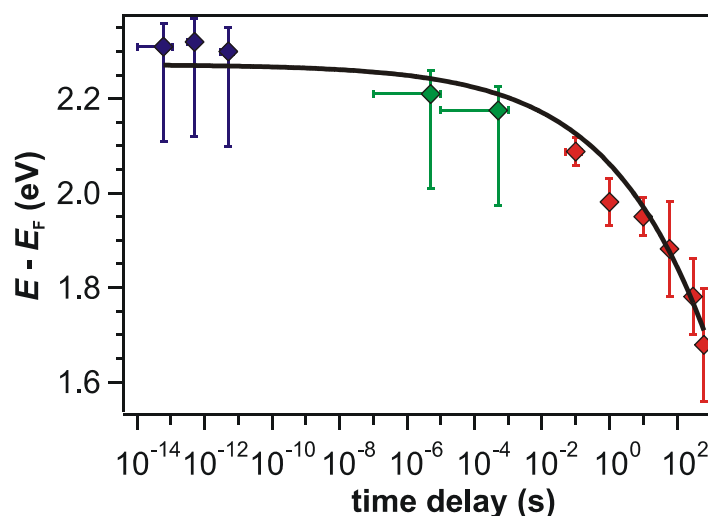
Furthermore, the observation of energetic stabilization of 0.6 eV within 10 min has implications for the discussion concerning the treatment of the early time dynamics of excess electrons in amorphous ice layers: In paragraph 4.1.4 the handling of just-photoinjected electrons as fully equilibrated, Boltzmann-distributed species was questioned. As in the case of crystalline ice, the trapped excess electrons continue to be stabilized over 17 orders of magnitude in time, it can be concluded that they have not reached – even after minutes – their potential minimum. The assumption of fully equilibrated solvated electrons in amorphous D_2O after 1 ps is thus doubtable.

In any case, the transition to crystalline ice enables the investigation of electron solvation dynamics over a range of 17 orders of magnitude in time. The next paragraph will introduce the concept of a "stretched" exponential model, which allows for the explanation of the variety of timescales by the increasing dimensionality of the system. Moreover, it will be shown that electron stabilization is thermally activated. A model description will be developed, which facilitates – in combination with DFT calculations – understanding of collective and microscopic rearrangement of the solvent molecules.

4.2.2 Thermally Activated Electron Solvation via Conformational Substates

The dynamic evolution of the trapped electron's binding energy over a large range of timescales results from the high complexity of the solvent-solute system. With increasing solvation a higher number of solvent molecules in outer solvation shells are involved in the stabilization process. A widely accepted approach to the dynamics of highly complex systems is the stretched exponential function. [Koh63, Wil70, Fra91, Ans92, Zha96, Fra02] Invented by F. Kohlrausch in 1863 for the description of dielectric relaxation rates in polymers, [Koh63] it has been used for the characterization of a variety of different phenomena such as protein folding in aqueous solutions [Fra02] or mechanical creep in glassy fibers [Wil70]. The stretched exponential takes into account the system's increase of complexity by "stretching" the time in a simple rate equation by introducing the exponent β:

$$\frac{\partial q}{\partial \left(t^{\beta} \right)} = g \cdot \left(q - q_0 \right) \qquad \text{with} \qquad 0 < \beta < 1 \tag{4.16}$$

The change of the solvent coordinate q as a function of stretched time t^{β}, is proportional to q-q_0 with the constant g. For the description of protein motions in aqueous solutions [Fra02], for example, the complexity of the system is increased due to the increased numbers of solvent molecules contributing to the solvation shell of the protein. As electrons, which are investigated in the present work, are the simplest conceivable solutes, the stretched exponential approach is appropriate for the description of the stabilization dynamics of the long-living trapped electrons in crystalline ice, which exhibit dynamics over a wide range of timescales. In addition to the stretched exponential behavior, the hydration of macromolecules evolves via so-called *conformational substrates* (CSS). The biomolecule is – in any (sub-)state of solvation – surrounded by a cavity of solvent molecules. Depending on the degree of solvation, the solvent is arranged in a certain *conformation*. As sketched in the left panel of Fig. 4.29, different CSS, introduced by the reorientation of one solvent molecule from conformation p_A to p_B, result in different potential energies E_A and E_B of the solvent-solute system and are separated by potential barriers. The activated character of transmission from one CSS to the other results in a significant temperature dependence. [Ans01, Jäg01] It is assumed that the progression across the substates is a thermally activated process, leading to a temperature-dependent proportionality factor in the rate equation (4.16) of

$$g(T) = \left(\frac{\exp\left[-\frac{E_a}{k_B T} \right]}{\tau_0} \right)^{\beta} \tag{4.17}$$

where E_a describes the barrier between the conformational substates and τ_0 the characteristic time for the transition. The solution of (4.16) is:

$$q(t,T) = q_0 \cdot \left\{ 1 - \exp\left[-\exp\left[-\frac{E_a}{k_B T} \right] \cdot \left(\frac{t}{\tau_0} \right)^{\beta} \right] \right\} \tag{4.18}$$
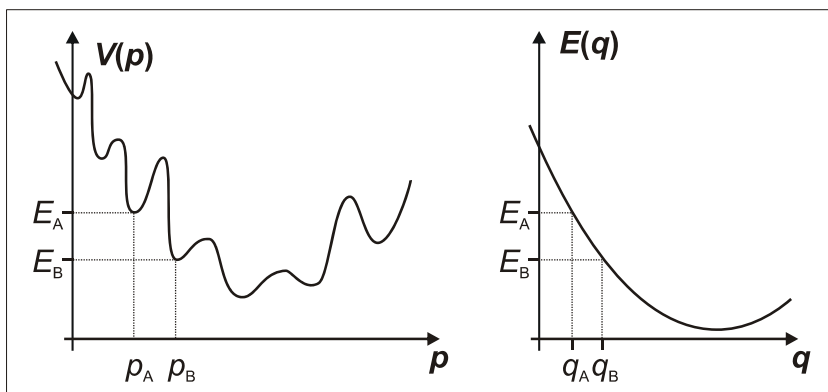

Fig. 4.29: *Conformational Substates.* The system has to overcome potential barriers for solvation to proceed via CSS. The potential minima, i.e. the quasi-equilibrium binding energy of the sum of all trapped electrons, follow a harmonic potential considering collective stabilization. See text for details.
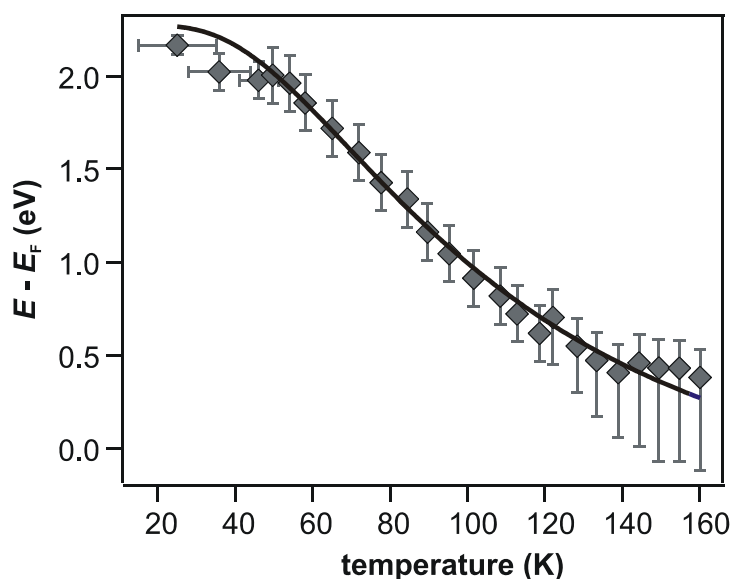
Fig. **4.30**: *Temperature Dependence of the Trapped Electrons.* The shift of the e_T maximum is plotted as a function of sample temperature and shifs down to the Fermi Level upon heating from 25 K to 160 K. Solid line results from the conformational substates model based on a stretched exponential approach as introduced in the text (data adopted from [Gah04]).

It was shown in [Gah04] that the ultralong-living trapped electrons in crystalline D_2O/Ru(001) indeed exhibit a strong dependence on temperature, as depicted in Fig. 4.30. The maximum of the e_T peak shifts by almost 2 eV to lower energies upon a temperature increase from 25 to 160 K.[90] The stabilization dynamics of the trapped electrons in crystalline ice therefore depend significantly on temperature, as expected for a system following the stretched exponential behavior via conformational substates. The application of the above described theoretical approach is thus reasonable. As described by equation (4.18), the progression of the system along the global solvent coordinate q is thermally activated. A harmonic potential is assumed to describe the binding energy gain of the trapped electrons with on-going solvation:

$$E(q) = A \cdot (q - q_0)^2 + E_0 \tag{4.19}$$

In contrast to the Marcus Theory (cf. section 2.1), where the harmonic potential resulted from the assumption that the reorientations of the solvent molecules are in the linear response limit, $E(q)$ describes here only the *potential minima* of distinct CSS. These substates are separated by potential barriers, which have to be overcome to proceed along q. Fig. 4.29 depicts the *local* potential as a function of another reaction coordinate p (left panel), which takes into consideration the thermally activated motion along the *global* coordinate q. Along p, the potential V exhibits several potential barriers, which separate the different CSS. The corresponding q-values can be extracted from the right panel of Fig. 4.29. Considering only *one* trapped electron, the solvation occurs therefore in discrete steps. However, as a *distribution* of electrons is observed in the experiment, each electron experiences slightly different environments leading to varying binding energies and substates, the collective motion can be described by a harmonic potential along q. The time and temperature dependence of the e_T peak hence results from (4.18) and (4.19):

---

[90] The peak maximum was extracted from UV only spectra, such as shown in Fig. 4.23.

$$E(t,T) = A \cdot q_0^2 \cdot \exp\left[-2 \cdot \exp\left[-\frac{\beta \cdot E_a}{k_B T} \right] \cdot \left(\frac{t}{\tau_0} \right)^{\beta} \right] + E_0 \qquad (4.20)$$

Applying the above function to both, the time-dependent (Fig. 4.28) and the temperature-dependent e_T peak shift (Fig. 4.30) simultaneously, leads to excellent fits as indicated by the solid lines in the respective figures. The resulting parameters are given in Tab. 4.02.[91] It is noteworthy that both, activation barrier E_A and characteristic time τ_0, are averaged values originating from the manifold of species in the e_T distribution. Furthermore, these parameters describe the *local*, *microscopic* situation without considering the complexity increase of the system due to β. For example, the *global* barrier $\beta \cdot E_a = 16(1)$ meV is lower than E_a alone. The probability for a transition of the system to the next CSS is higher, when the manifold of molecules contributing to the solvation shell is considered and the barrier becomes effectively smaller than the activation energy of solely one elementary reaction step (transition between individual CSS). The characteristic time $\tau_0 = 4$ ms is long compared with typical vibrational frequencies. This observation suggests that correlation among the individual microscopic processes plays a relevant role for the screening of the excess electron. The stretching exponential β is a measure of the "internal clock" of the system, which is synchronized by transition events between CSS. The ultrafast dynamics are stretched in comparison to the macroscopic timescale. The amplitude A and the minimum E_0 define the shape of the harmonic potential along q, revealing the beginning (i.e. binding energy right after electron trapping) and the end of electron solvation (i.e. perfectly solvated electron) with 2.25 eV and -0.75 eV, respectively.

A	3.0(1) eV
E_a	96(5) meV
τ_0	4(1) ms
β	0.16(3)
E_0	-0.75(10) eV

Tab. 4.02: *Parameters of CSS Model.*

In collaboration with A. Rubio and coworkers, who perform *ab initio* DFT calculations, possible candidates for electron trapping sites and conformational substates where developed. According to Xe overlayer experiments (similar to those introduced in 4.1.3), the trapped electrons reside on the surface of the adsorbed ice. [Gah04, Bov07] In the present work, the pre-existence of these traps has been shown as discussed above on the basis of Fig. 4.27. Hence Rubio *et al.* performed first-principle calculations using a plane wave supercell consisting of a 4x4 surface cell of ice $I_h(0001)$ in six layers (cf. 2.4.1) and a vacuum region corresponding to 10 layers.[92] This rather large unit cell was necessary to achieve lateral electron localization at defect sites.[93] Fig. 4.31a presents the geometry of the ice surface and shows exemplary orientational

---

[91] The global coordinate q was scaled with $q_0 = 1$.

[92] Troullier-Martins pseudopotentials with a plane wave energy cut-off of 80 Ry and the Becke-Lee-Yang-Parr (BLYP) exchange correlation energy functional were employed, which are known to describe water systems well. [Bal05] These parameters provide a good accuracy for the electronic and structural properties, which is required, as small dipole-induced structural rearrangements are investigated.

[93] A "complete" DFT calculation including the metal substrate is too complex to perform with sufficient accuracy. As the long lifetime of the electrons is a proof for perfect screening from the substrate, the theoretical results are certainly comparable to the experimental data.

defects S_1 and S_A. Rubio et al. calculated the formation energies E_{form} for various types of surface defects and found that the most favorable orientational defect site – if only one molecule contributes to the defect – is the S_A-flip (E_{form} = 0.25 eV) of the topmost layer, which is accompanied by a reconstruction of the undercoordinated D_2O neighbor S_2. The nearest neighbor of the subsurface layer S_1 subsequently gives rise to another orientational defect with different formation energies (0.45 eV). Electrons localize laterally in these kinds of defects (Fig. 4.31c) and their electron density remains almost completely outside of the ice as depicted in panel (e) for the S_A-flip. The electron typically gains 100 meV of energy upon binding to a defect site. [Bov07] Structural relaxation contributes 60 meV. Hence, the energetic shift observed in the 2PPE measurement cannot solely result from equilibrating in the present CSS, but must involve further thermally activated reconstruction.
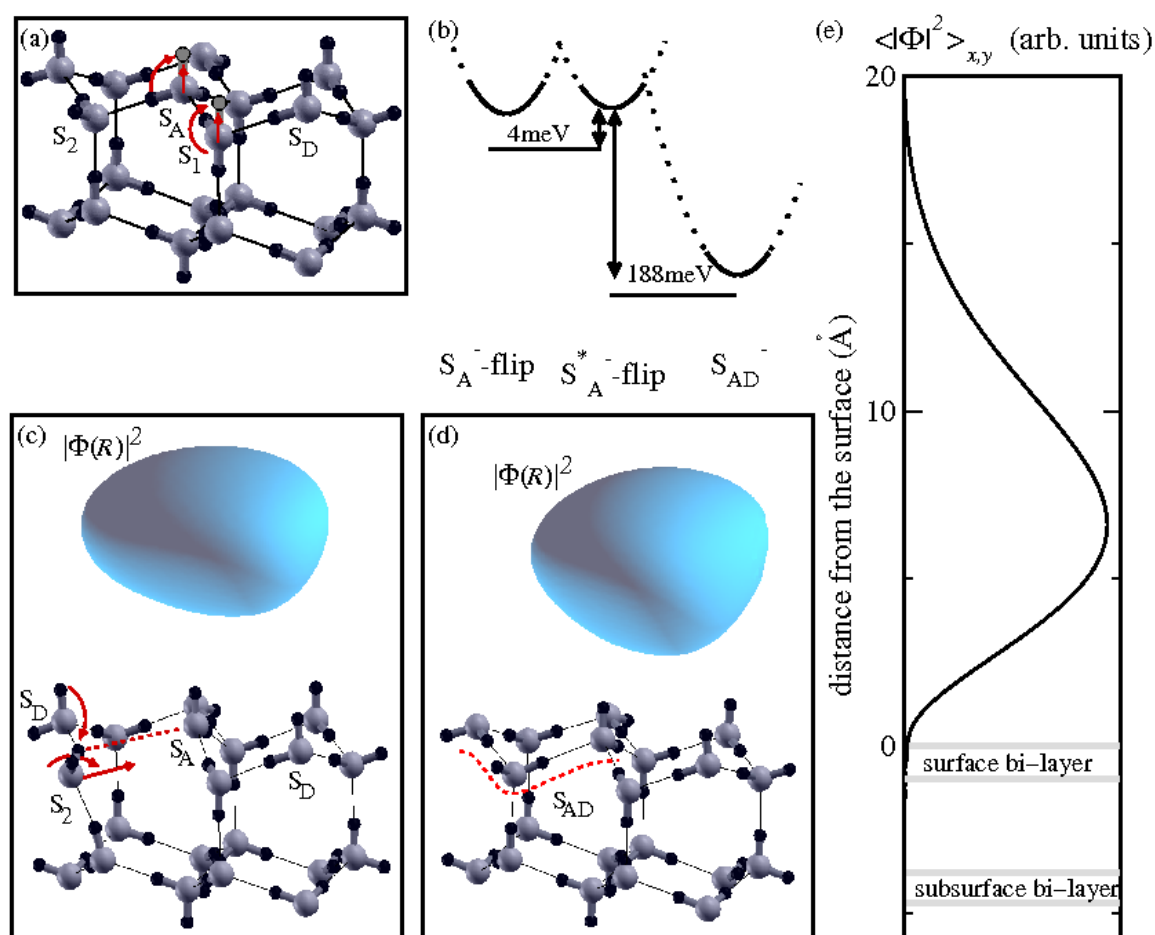

Fig. 4.31: *DFT Calculation of Orientational Defect Sites for Electron Trapping.* a) Arrows indicate the formation of S_A- and S_1-flip at the ice surface. b) Energies of exemplary orientational defects. c) Geometry of S_A-flip and excess electron density at 70% of its maximum value; note the large movement of S_A and its neighbour away form the ideal sites. The reconstructions of the H-bonded network for the S_{AD} formation are indicated by the arrows. (d) Geometry of S_{AD} and the excess electron density as for S_A-flip; the dashed line indicates new hydrogen bonds. (e) In-plane average of the density of the excess electron vs. the distance from the surface at S_A-flip. The negligible overlap with the ice/metal system (similarly for the S_{AD} defect) becomes apparent. The gray horizontal lines indicate the position of the oxygen lagers.

As the defects discussed above are governed by broken H-bonds and undercoordination of molecules, Fig. 4.31d depicts a complex of orientational defects, were the natural hydrogen-bonded network is restored. As in the case of the S_a-flip, the electron is bound to two DO-bonds, as apparent from Fig. 4.31c and Fig. 4.31d. The steps of the re-coordination are indicated by the arrows in Fig. 4.31c. Gyration of S_2 maintains its three-fold coordination (S^*_A-flip). The hydrogen bond between S_2 and S_D is maintained by reorientation of S_D and S_A. This formation of the defect S_{AD} leads to a binding energy gain of the trapped electron of 0.19 eV. It is remarkable that the reorientation from S_A-flip to S_{AD} has a *negative* formation energy (-40 meV) if the excess electron is present. Rubio *et al.* could also show that further reorientation of the neighboring molecules and comparable reconstructions in the subsurface layers lead not only to an enhancement of the electron's binding energy but also to further localization parallel to the surface. Currently, coalescence of defects and subsequent mutual reorientations leading to configurations with larger binding energies are investigated to reproduce the complete change in bindinge energy of the excess electrons observed by 2PPE. [Rub07] The progression across such conformational substates must be thermally activated as the corresponding potential minima are separated by energy barriers.[94]

In conclusion, density functional theory could identify probable candidates for conformational substates. The excellent reproduction of the 2PPE data by the stretched exponential approach including CSS, yielded a mean activation barrier of ~100 meV, which is in good agreement with the formation energies and binding energy gain of excess electrons found using DFT.

The description of electron solvation using a harmonic potential leading to equation (4.20) however, enables interpretation of the phenomenon from a different point of view. Exchanging the "real time" with the "internal clock" of the system $\tau = t^{\beta}$, (4.20) may be rewritten as

$$E(\tau, T) = A \cdot \left(q_0 \cdot \exp\left[-\rho(T) \cdot \tau\right]\right)^2 + E_0. \tag{4.21}$$

This expression is reminiscent of the time evolution of the potential energy of a damped harmonic oscillator, where

$$E_{pot}(t) = \frac{k}{2} \cdot x^2(t) \tag{4.22}$$

and

$$x(t) = x_0 \cdot e^{-\rho \cdot t} \cdot \cos \omega t \approx x_0 \cdot e^{-\rho \cdot t} \qquad \text{for} \qquad \rho \gg 1. \tag{4.23}$$

The stabilization dynamics of trapped electrons in crystalline ice can therefore be viewed as the relaxation of an over-damped harmonic oscillator with a temperature-dependent friction coefficient $\rho(T)$. This friction results from the progression of the system across the above

---

[94] As such orientational defects certainly also occur in amorphous ice, the question arises, why ultralong-living electrons are not observed for these interfaces. Persumably, the additional long-range disorder in the amorphous adlayers to a faster electron decay and prohibits the formation of the photostationary state, which enables the observation of low-intensity feature of the trapped electrons in crystalline ice in the first place.

described conformational substates. To fulfill energy conservation, the binding energy gain (4.20) leads to an energy dissipation to the solvent of

$$E_{dissi}(\tau,T) = A \cdot \left(1 - q_0 \cdot \exp[-\rho(T) \cdot \tau]\right)^2 . \tag{4.24}$$

Conclusions

The above developed description of the energetic shift of the trapped electron distribution e_T allows the following interpretation of the observed course of events: After photoexcitation of hot metal electrons and charge injection into the ice adlayer via the delocalized $n = 1$ image potential state, the electrons localize in pre-existing traps in the adlayer, identified to be orientational defects at the ice-vacuum interface. The electrons gain almost one eV in binding energy within 16 fs. Being well-screened from the metal substrate, the ultralong lifetime of the excess electrons allows observation of their solvation dynamics over a range of 17 orders of magnitude in time. The energetic stabilization slows down significantly with increasing time and exhibits a strong temperature dependence, so that the equilibration, "freezing", of the excess electrons is well-described by a stretched exponential function including a temperature-dependent friction coefficient. The damping of the electron relaxation occurs due to activated progression across conformational substates, separated by energy barriers. Employing this model description, average microscopic barrier heights of 96 meV were found, agreeing with the formation energies for orientational defects calculated by DFT.

The performance of high-statistic measurements and the development of new, systematic data analysis procedures revealed the femtosecond formation dynamics of the trapped electrons and enabled observation of electron solvation over 17 orders of magnitude in time. In combination with sophisticated ab initio DFT calculations, probable trapping sites and conformational substates were uncovered. The present study thus developed deeper understanding of the microscopic *and* collective processes involved.

Recalling the detailed investigation of *amorphous* ice-metal interfaces in section 4.1, it can be concluded that the electron transfer and solvation dynamics at ice-metal interfaces incorporate a large variety of appearances: Strong and weak coupling, surface and bulk solvation, ultrafast and ultraslow dynamics, solvation due to structural relaxation and via conformational substates. The diversity of phenomena of the ice-metal systems investigated allowed for systematic comparison of related interfaces, leading to deeper insight into heterogeneous charge transfer and electron solvation. However, for comprehensive understanding, the influence of the solvent has to be revealed. The next chapter presents results on the electron transfer and solvation dynamics at the $NH_3/Cu(111)$ interface, showing that the right choice of adsorbate can even allow for a tuning of the degree of coupling strength.